



### **Science Arts & Métiers (SAM)**

is an open access repository that collects the work of Arts et Métiers Institute of Technology researchers and makes it freely available over the web where possible.

This is an author-deposited version published in: <https://sam.ensam.eu>  
Handle ID: <http://hdl.handle.net/10985/17841>

#### **To cite this version :**

Bernd R. NOACK, Steven L. BRUNTON, Jean-Christophe LOISEAU - Sparse reduced-order modelling: sensor-based dynamics to full-state estimation - Journal of Fluid Mechanics - Vol. 844, p.459-490 - 2018

Any correspondence concerning this service should be sent to the repository

Administrator : [scienceouverte@ensam.eu](mailto:scienceouverte@ensam.eu)



# Sparse reduced-order modeling: Sensor-based dynamics to full-state estimation

Jean-Christophe Loiseau<sup>1†</sup>, Bernd R. Noack<sup>2,3,4</sup> and Steven L. Brunton<sup>5</sup>

<sup>1</sup>Laboratoire DynFluid, Arts et Métiers ParisTech, 75013 Paris, France

<sup>2</sup>Laboratoire d'Informatique pour la Mécanique et les Sciences de l'Ingénieur, LIMSI-CNRS, Rue John von Neumann, Campus Universitaire d'Orsay, Bât 508, F-91403 Orsay, France

<sup>3</sup>Institut für Strömungsmechanik, Technische Universität Braunschweig, Hermann-Blenk-Straße 37, D-38108 Braunschweig, Germany

<sup>4</sup>Institut für Strömungsmechanik und Technische Akustik (ISTA), Technische Universität Berlin, Müller-Breslau-Straße 8, D-10623 Berlin, Germany

<sup>5</sup>Department of Mechanical Engineering, University of Washington, Seattle, WA 98195, USA

We propose a general dynamic reduced-order modeling framework for typical experimental data: time-resolved sensor data and optional non-time-resolved PIV snapshots. This framework contains four steps. First, the sensor signals are lifted to a dynamic feature space. Second, we identify a sparse human-interpretable nonlinear dynamical system for the feature state based on the sparse identification of nonlinear dynamics (SINDy). Third, if PIV snapshots are available, a local linear mapping from the feature state to velocity fields is shown to be orders of magnitudes more accurate than optimal modal expansions of the same order. Fourth, a generalized feature-based modal decomposition identifies coherent structures that are most dynamically correlated with the linear and nonlinear interaction terms in the sparse model, adding interpretability. Steps 1 and 2 define a black-box model. Optional steps 3 and 4 lift the black-box dynamics to a ‘gray-box’ model of the coherent structures, if non-time-resolved full-state data is available. This gray-box modeling strategy is successfully applied to the transient and post-transient laminar cylinder wake, and compares favorably with a POD model. We foresee numerous applications of this highly flexible modeling strategy, including estimation, prediction and control. Moreover, the feature space may be based on intrinsic coordinates, which are unaffected by a key challenge of modal expansion: the slow change of low-dimensional coherent structures with changing geometry and varying parameters.

## 1. Introduction

Understanding and modeling complex fluid flows is a central focus in many scientific, technological, and industrial applications, including energy (e.g., wind, tidal, and combustion), transportation (e.g., planes, trains, and automobiles), security (e.g. airborne contamination), and medicine (e.g., artificial hearts and artificial respiration). Improved models of engineering flows have the potential to dramatically improve performance in these systems through optimization and control, resulting in practical gains such as drag reduction, lift increase, and mixing enhancement (Fabbiane *et al.* 2014; Brunton & Noack 2015; Sipp & Schmid 2016; Rowley & Dawson 2016). Although the Navier-Stokes equations provide a detailed mathematical model, this representation may be difficult to

† Email address for correspondence: loiseau.jc@gmail.com

use for engineering design, optimization, and control. Feynman *et al.* (2013) points out the limitation of the governing equations to reveal underlying behavior:

“The test of science is its ability to predict. Had you never visited the earth, could you predict the thunderstorms, the volcanos, the ocean waves, the auroras, and the colorful sunset?”

Instead of studying the Navier-Stokes equations directly, fluid systems are commonly discretized into a high-dimensional, nonlinear dynamical system with many degrees of freedom and multi-scale interactions. These equations are expensive to simulate, making them unwieldy for iterative optimization or in-time control, and they may also obscure the underlying physics, which often evolves on a low-dimensional attractor (Holmes *et al.* 2012; Noack *et al.* 2003). The various fidelities of model description were described by Wiener (1948): ‘white-box’ describes an accurate evolution equation based on first principles (e.g., Navier-Stokes discretization), ‘gray-box’ describes a low-dimensional model approximating the full state (e.g., POD-Galerkin models), and ‘black-box’ describes input-output models that lack a connection to the full state space (e.g., neural networks).

In the following, we outline related reduced-order models as our point of departure in §1.1 and foreshadow proposed innovations of this study in §1.2.

### 1.1. Related reduced-order models as point of departure

Reduced-order models provide minimal descriptions of the underlying fluid behavior in a compact and computationally efficient representation. There are many techniques for reduced-order modeling, ranging from physical reductions to purely data-driven methods, and nearly everything in between. Proper orthogonal decomposition (POD) (Sirovich 1987; Berkooz *et al.* 1993; Holmes *et al.* 2012) provides a low-rank modal decomposition of fluid flow field data, extracting the most energetic modes. It is then possible to Galerkin project the Navier-Stokes equations onto these modes, resulting in an approximate, low-dimensional model in terms of mode coefficients (Noack *et al.* 2011; Carlberg *et al.* 2015). POD-Galerkin models are widely used, as they are interpretable, gray-box models, and it is straightforward to reconstruct the high-dimensional flow field from the low-dimensional model via POD modes. The first pioneering example of Aubry *et al.* (1988) features wall turbulence—almost three decades ago. Subsequent POD models have been developed for the transitional boundary layer (Rempfer & Fasel 1994), the mixing layer (Ukeiley *et al.* 2001; Wei & Rowley 2009), the cylinder wake (Deane *et al.* 1991; Galletti *et al.* 2004), and the Ahmed body wake (Östth *et al.* 2014), to name only a few.

POD-Galerkin modeling is challenging for changing domains (Bourguet *et al.* 2011), changing boundary conditions (Graham *et al.* 1999) and slow deformation of the modal basis (Babae & Sapsis 2016). Standard Galerkin projection can also be expected to suffer from stability issues (Rempfer 2000; Schlegel & Noack 2015; Carlberg *et al.* 2017), although including energy-preserving constraints may improve the long-time stability and performance of nonlinear models (Balajewicz *et al.* 2013; Cordier *et al.* 2013). POD-Galerkin models tend to be valid for a narrow range of operating conditions, namely around the data set used for the POD modes. Transients also pose a challenge to POD modeling. Noack *et al.* (2003) and Tadmor *et al.* (2010) demonstrate the ability of a low-dimensional model to reproduce nonlinear transients of the von Kàrmàn vortex shedding past a two-dimensional cylinder, provided the projection basis includes a *shift mode* quantifying the distortion between the linearly unstable base flow and marginally stable mean flow. These techniques have been extended to include the effect of wall actuation (Graham *et al.* 1999; Rediniotis *et al.* 2002).

In addition to the physics-based Galerkin projection, data-driven modeling approaches

are prevalent in fluid dynamics (Brunton & Noack 2015; Rowley & Dawson 2016). For example, dynamic mode decomposition (DMD) (Schmid 2010; Rowley *et al.* 2009; Kutz *et al.* 2016), the eigensystem realization algorithm (ERA) (Juang & Pappa 1985), Koopman analysis (Mezić 2005, 2013; Tu *et al.* 2014; Williams *et al.* 2015), cluster-based reduced order models (CROM) (Kaiser *et al.* 2014), NARMAX models (Billings 2013; Semeraro *et al.* 2016; Zhang *et al.* 2012; Glaz *et al.* 2010), and network analysis (Nair & Taira 2015) have all been used to identify dynamical systems models from fluids data, without relying on knowledge of the underlying Navier-Stokes equations. DMD models are readily obtained directly from data, and they provide interpretability in terms of flow structures, but the resulting models are linear, and the connection to nonlinear systems is tenuous unless DMD is enriched with nonlinear functions of the data (Williams *et al.* 2015; Kutz *et al.* 2016). Neural networks have long been used for flow modeling and control (Milano & Koumoutsakos 2002; Zhang & Duraisamy 2015; Lee *et al.* 1997; Krizhevsky *et al.* 2012), and recently deep neural networks have been used for Reynolds averaged turbulence modeling (Ling *et al.* 2016; Kutz 2017). Parsimony has also become an overarching theme when using machine learning to model nonlinear dynamics. Bongard & Lipson (2007) and Schmidt & Lipson (2009) discover governing dynamics and conservation laws using genetic programming along with a Pareto analysis to balance model accuracy and complexity. However, some machine learning methods, such as neural networks and genetic programming, may be prone to overfitting, have limited interpretability, and make it difficult to incorporate known physical constraints.

Recently, Brunton *et al.* (2016b) introduced the sparse identification of nonlinear dynamics (SINDy), which identifies parsimonious nonlinear models from data. SINDy follows the principle of Ockham’s razor, resting on the assumption that there are only a few important terms that govern the dynamics of a system, so that the equations are sparse in the space of possible functions. Sparse regression is then used to efficiently determine the fewest terms in the dynamics required to accurately represent the data, preventing overfitting. Because SINDy is based on linear algebra (i.e., the nonlinear dynamics are represented as a linear combination of candidate nonlinear functions), the method is readily extended to incorporate known physical constraints (Loiseau & Brunton 2016). In general, it is possible to obtain nonlinear models using genetic programming or SINDy on POD or DMD mode coefficients, which make these methods *gray box*, having a transformation from the model back to the high-dimensional, interpretable state-space. However, models developed on POD/DMD mode coefficients may still suffer from fundamental challenges of traditional POD-Galerkin models, such as capturing changing boundary condition, moving geometry, and varying operating condition.

## 1.2. Contribution of this work

In this work, we introduce a new gray-box modeling procedure that yields interpretable nonlinear models from measurement data. The method is applied to the well-investigated two-dimensional transient flow past a circular cylinder with slow change of the base flow and varying coherent structures (Tadmor *et al.* 2011). In particular, we develop nonlinear models only from lift measurements that accurately capture steady-state and transient flow behavior. First, a feature vector is constructed from the lift signal, including a time-delayed value. Second, a sparse dynamical model is identified in this feature space. For the following steps, full-state measurement data is assumed to be available. Third, a local linear mapping from feature vector to velocity field is constructed using a K-nearest neighbors (KNN) approach. This mapping provides significantly more accurate flow reconstruction, as compared to a POD-Galerkin model of the same order. Technically, we mitigate the significant challenges of using an ‘elliptic’ Galerkin modeling approach

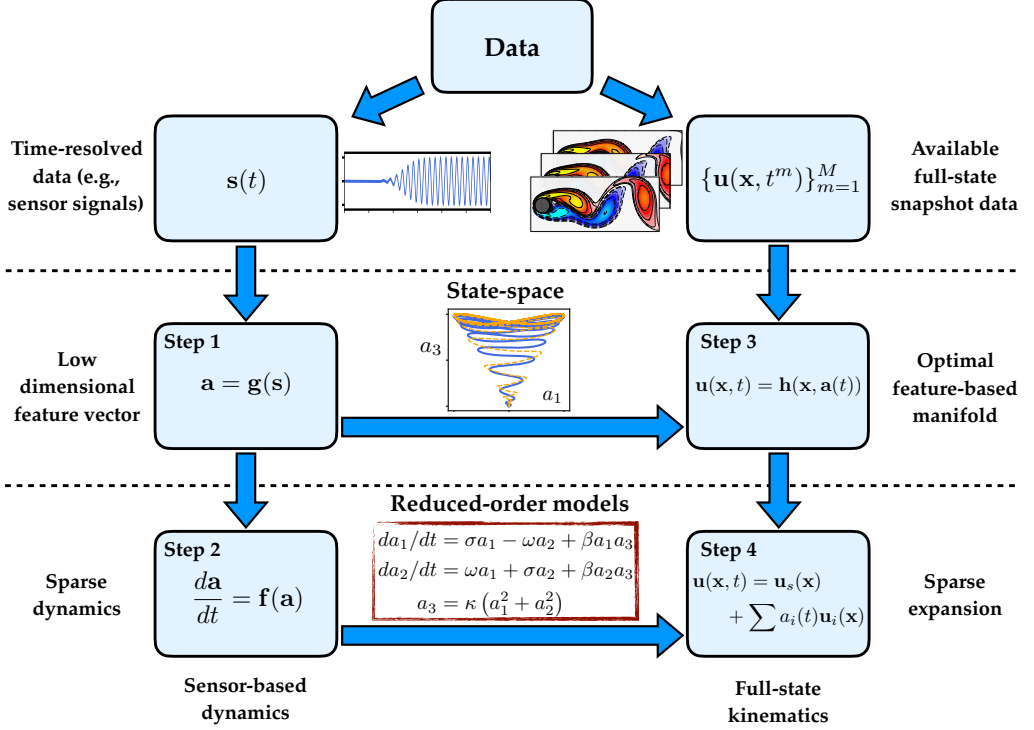


FIGURE 1. Schematic overview of the proposed sparse modeling procedure. A sparse dynamical system (Brunton *et al.* 2016b) is identified based on features obtained from sensor signals  $\mathbf{s}$ , and the full state  $\mathbf{u}$  may also be estimated with the availability of PIV snapshots (optional).

to an ‘hyperbolic’ dynamics: The global modes connect all locations in all directions instantaneously while the coherent structures are convected with the flow (Noack 2016).

Furthermore, it is also possible to construct a generalized set of modes that are most dynamically correlated with the given terms in the identified model. The resulting modal decomposition is similar in concept to DMD, although the present approach corrects linear modes for the effect of nonlinearity and also reveals entirely new structures associated with given nonlinear interaction terms. With the associated full-state data and generalized modes, it is possible to reconstruct the full-state associated with a given low-dimensional prediction in the reduced-order gray-box model.

To summarize, the resulting gray-box modeling procedure has the following beneficial features: (i) it captures nonlinear physics, (ii) it is based on a simple, non-invasive computational algorithm, (iii) the resulting model is interpretable in terms of nonlinear interaction physics and generalized modes (optional with full-state data), and (iv) modeling feature vectors is more robust to mode deformation, moving geometry, and varying operating condition. This procedure is shown schematically in figure 1.

The manuscript is organized as follows: §2 provides an overview of the flow configuration considered in this work, namely the incompressible, two-dimensional flow past a circular cylinder at  $Re = 100$ . §3 describes the proposed gray-box modeling procedure, including modeling in feature space and obtaining a generalized modal expansion if full-state data is available. In §4, numerical results for the gray-box modeling procedure are presented and analyzed for the cylinder flow. Finally, §5 summarizes our key findings and provides the reader with possible future directions to extend this work.

## 2. Flow configuration

The flow configuration considered in the present work is the two-dimensional incompressible viscous flow past a circular cylinder at  $Re = 100$ . This Reynolds number, based on the free-stream velocity  $U_\infty$ , the cylinder diameter  $D$  and the kinematic viscosity  $\nu$ , is well above the onset of vortex shedding (Zebib 1987; Schumm *et al.* 1994) and below the onset of three-dimensional instabilities (Zhang *et al.* 1995; Barkley & Henderson 1996). In the fluid dynamics community, a large body of literature exists in which this particular setup has been chosen to illustrate modal decomposition (Bagheri 2013) and model identification techniques (Noack *et al.* 2003; Sengupta *et al.* 2015; Brunton *et al.* 2016b; Rowley & Dawson 2016). This setup is thus a particularly compelling test case to illustrate our model identification strategy, as well as to draw connections and quantify its performance against other well-established techniques.

The dynamics of the flow are governed by the incompressible Navier-Stokes equations

$$\begin{aligned} \frac{\partial \mathbf{u}}{\partial t} + (\mathbf{u} \cdot \nabla) \mathbf{u} &= -\nabla p + \frac{1}{Re} \nabla^2 \mathbf{u} \\ \nabla \cdot \mathbf{u} &= 0, \end{aligned} \quad (2.1)$$

where  $\mathbf{u} = (u, v)^T$  and  $p$  are the velocity and pressure fields, respectively. The center of the cylinder has been chosen as the origin of the reference frame  $\mathbf{x} = (x, y)$ , where  $x$  denotes the streamwise coordinate and  $y$  denotes the spanwise coordinate. This study considers the same computational domain as in Noack *et al.* (2003), extending from  $x = -5$  to  $x = 15$  in the streamwise direction, and from  $y = -5$  to  $y = 5$  in the spanwise direction. A uniform velocity profile is prescribed at the inflow, a classical stress-free boundary condition is used at the outflow, and free-slip boundary conditions are used on the lateral boundaries of the computational domain. Based on the spectral element solver Nek 5000 (Fischer *et al.* 2008), the domain is discretized by 1832 seventh-order spectral elements. Finally, the time-integration of the diffusive terms relies on a Backward Differentiation of order 3 (BDF3), while the convective terms are advanced in time based on a third-order accurate extrapolation.

Many of the direct numerical simulations performed in this work have been initialized with the following initial condition

$$\mathbf{u}(\mathbf{x}, 0) = \mathbf{u}_s(\mathbf{x}) + 0.001\boldsymbol{\epsilon}(\mathbf{x}), \quad (2.2)$$

where  $\mathbf{u}_s(\mathbf{x})$  is the linearly unstable steady solution of the Navier-Stokes equations and  $\boldsymbol{\epsilon}(\mathbf{x})$  is a zero-mean and unit-variance random white-noise velocity field. Each simulation is run for 150 convective time units, providing  $M = 1200$  equidistantly sampled velocity snapshots  $\mathbf{u}^m(\mathbf{x}) = \mathbf{u}(\mathbf{x}, t^m)$ ,  $m = 1, \dots, M$ , and associated measurements of the lift and drag coefficients,  $C_L(t^m)$  and  $C_D(t^m)$ . This time-span covers the entire unforced transient phase, from the steady solution to the fully developed von Kármán vortex street. Figure 2 depicts a typical evolution of the lift coefficient  $C_L$ , while figure 3 shows snapshots of the vorticity field at different instants of time. For  $t \leq 50$ , the flow is governed by linear dynamics. Consequently, the vorticity field of the perturbation  $\mathbf{v}(\mathbf{x}, t) = \mathbf{u}(\mathbf{x}, t) - \mathbf{u}_s(\mathbf{x})$ , as shown in figure 3(a), can be well approximated by the leading instability mode. For  $50 \leq t \leq 80$ , the perturbation grows to an extent that nonlinear effects cause the perturbation to distort. Eventually, for  $t \geq 80$ , the flow settles onto a periodic limit cycle corresponding to the onset of the von Kármán vortex street. Given the evolution of the lift coefficient depicted in figure 2 and the associated snapshots shown in figure 3, the aim of the present work is to propose a new reduced-order modeling strategy able to

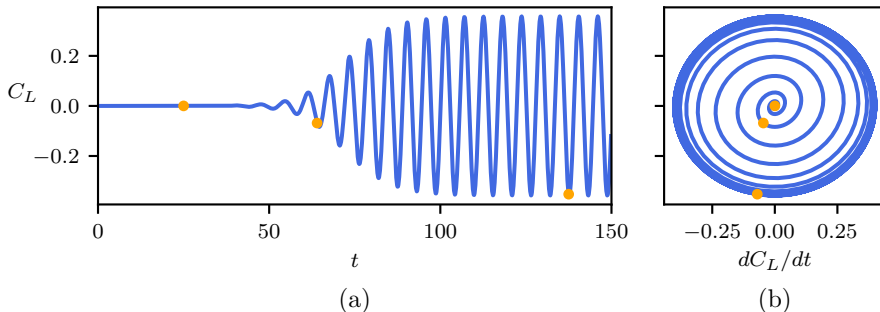


FIGURE 2. (a) Evolution of the lift coefficient  $C_L$  as a function of time for the two-dimensional cylinder flow at  $Re = 100$ . (b) Trajectory of the system in the phase-plane  $(C_L, dC_L/dt)$ . In both figures, the orange dots indicate the instants of time for which the corresponding vorticity field is shown in figure 3.

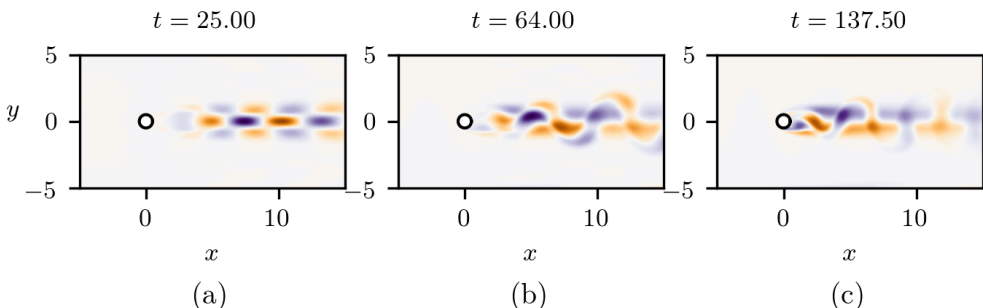


FIGURE 3. Snapshots of the vorticity field at the different time instants highlighted in figure 2. Note that the vorticity field of the linearly unstable baseflow,  $\mathbf{u}_s(\mathbf{x})$ , has been subtracted in order to highlight the vorticity induced by the perturbation.

accurately reproduce such dynamics and flow structures, but without the need for the full flow field or modes.

### 3. Sparse sensor-based modeling

Here, we discuss the core mathematical and algorithmic framework used to identify nonlinear reduced-order models and build a full-state estimator from data. The identification procedure relies on the *Sparse Identification of Nonlinear Dynamics* (SINDy) method (Brunton *et al.* 2016b) briefly summarized in §3.2. As a second step, we introduce the reader to two different full-state estimators in §3.3.

#### 3.1. From sensor signals to feature space

Experimentalists typically only have access to a limited number of time-resolved sensor measurements  $\mathbf{s}$ . In contrast, one can gather space-time resolved data at every single point within the computational domain when performing direct numerical simulations. The aim of the present work is to illustrate how one can leverage recent advances in system identification and machine learning to construct reduced-order models directly from limited sensor measurements. We mimic these experimental conditions with direct

numerical simulations. In the present work, we consider a sensor measurement given by

$$s := C_L(t), \quad (3.1)$$

where  $C_L$  is the lift coefficient. Note that in general  $\mathbf{s}$  may be a vector of measurements, for example including the lift and drag coefficients, pressure measurements on an immersed body, or point velocity field measurements at select locations; however, in the present study, we will show that lift is sufficient to characterize the flow. Given the sensor measurements  $\mathbf{s}$ , our aim is to identify a low-order model that allows us to predict the evolution of our system. However, the sensor measurements may need to be augmented, or *lifted*, to include functions of the sensor measurements. We consider the augmented state  $\mathbf{a}$  to be a feature vector given by

$$\mathbf{a} = \mathbf{g}(\mathbf{s}). \quad (3.2)$$

There are many choices for the mapping  $\mathbf{g}$  to enrich the sensor measurements and improve models. If the sensors are sufficient to define the state of the system, then  $\mathbf{g}$  may be the identity map. If the sensors consist of high-dimensional snapshots, then  $\mathbf{g}$  may extract POD mode coefficients. It may also be possible to augment the measurements with delay-embedding (Takens 1981; Juang & Pappa 1985; Brunton *et al.* 2017). More generally, choosing a good transformation,  $\mathbf{g}$ , is an important open problem, with connections to representation theory and the Koopman operator perspective on dynamical systems (Mezić 2005, 2013; Williams *et al.* 2015; Brunton *et al.* 2016a, 2017; Arbabi & Mezić 2016). In the present study, we choose  $\mathbf{g}$  to augment the sensor measurement of the lift coefficient with its time derivative, along with a proper scaling:

$$\begin{aligned} a_1 &:= s(t), \\ a_2 &:= \frac{1}{\omega_\infty} \frac{ds}{dt}(t), \end{aligned} \quad (3.3)$$

where  $\omega_\infty$  is the post-transient angular shedding frequency. This choice has been guided by physical considerations: the lift can be measured and allows for the characterization of the state of the flow. It is also well-known that the flow around a two-dimensional cylinder at  $Re = 100$  only necessitates three degrees of freedom (Noack *et al.* 2003), or features, to be approximately described: the shedding amplitude, shedding phase and the degree of base flow deformation. In this work, we will show that the degree of base flow deformation can be described by the drag coefficient, which is then modeled as an algebraic equation of the feature vector  $\mathbf{a}$ .

This setup mimics an experiment in Hosseini *et al.* (2016). The pressure difference between the top and bottom side of a cylinder is a surrogate quantity for the lift. This difference has been recorded in a time-resolved manner while non-time-resolved PIV flow snapshots were taken. The pressure difference and a flow estimator have been employed for a time-resolved estimate of the fluid flow field, comprising the base flow, von Kármán vortex shedding and the second harmonics. The analogues of  $a_1$  and  $a_2$  were the cosine and sine Morlet transforms of the pressure difference history.

### 3.2. Sparse Identification of Nonlinear Dynamics

Identifying reduced-order models from data is a central challenge in mathematical physics, with a rich history of developments in fluid dynamics. The form of the dynamics is typically either constrained via prior knowledge, as in the Galerkin projection, or a particular model structure is chosen heuristically, and parameters are optimized to match the data. Simultaneous identification of the model structure and parameters from data is



considerably more challenging, as there are combinatorially many possible model structures. The sparse identification of nonlinear dynamics (SINDy) architecture (Brunton *et al.* 2016b) bypasses the intractable combinatorial search through all possible model structures, leveraging the fact that many systems may be modeled by dynamics  $\mathbf{f}$  that are sparse in the space of possible right-hand side functions:

$$\frac{d\mathbf{a}}{dt} = \mathbf{f}(\mathbf{a}), \quad (3.4)$$

where  $\mathbf{a}$  is the same state vector as in §3.1. It is then possible to solve for the relevant terms that are active in the dynamics using either a convex  $\ell_1$ -regularized regression (Tibshirani 1996) or a sequentially thresholded least-squares (Brunton *et al.* 2016b); these algorithms penalize the number of terms in the dynamics and scale favorably to large problems.

First, time-series data is collected and formed into a data matrix:

$$\mathbf{A} = [\mathbf{a}(t^1) \quad \mathbf{a}(t^2) \quad \cdots \quad \mathbf{a}(t^M)]^T \quad (3.5)$$

where ‘ $T$ ’ denotes the matrix transpose. A similar matrix of derivatives is formed:

$$\dot{\mathbf{A}} = \left[ \frac{d\mathbf{a}}{dt}(t^1) \quad \frac{d\mathbf{a}}{dt}(t^2) \quad \cdots \quad \frac{d\mathbf{a}}{dt}(t^M) \right]^T. \quad (3.6)$$

In practice, this may be computed directly from the data in  $\mathbf{A}$ . However, for noisy data, the total-variation regularized derivative (Chartrand 2011) tends to provide numerically robust derivatives. Based on the data in  $\mathbf{A}$ , a library of candidate nonlinear functions  $\Theta(\mathbf{A})$  is constructed:

$$\Theta(\mathbf{A}) = [1 \quad \mathbf{A} \quad \mathbf{A}^2 \quad \cdots \quad \mathbf{A}^d \quad \cdots \quad \sin(\mathbf{A}) \quad \cdots]. \quad (3.7)$$

Here, the matrix  $\mathbf{A}^d$  denotes a matrix with column vectors given by all possible time-series of  $d$ -th degree polynomials in the state  $\mathbf{a}$ . The dynamical system in Eq. (3.4) may now be represented in terms of the data matrices in Eqs. (3.6) and (3.7) as

$$\dot{\mathbf{A}} = \Theta(\mathbf{A})\Xi. \quad (3.8)$$

Each column  $\Xi_k$  in  $\Xi$  is a vector of coefficients determining the active terms in the  $k$ -th row equation in Eq. (3.4). A parsimonious model will provide an accurate model fit in Eq. (3.8) with as few terms as possible in  $\Xi$ . Such a model may be identified using a convex  $\ell_1$ -regularized sparse regression:

$$\Xi_k = \underset{\Xi'_k}{\operatorname{argmin}} \|\dot{\mathbf{A}}_k - \Theta(\mathbf{A})\Xi'_k\|_2 + \lambda \|\Xi'_k\|_1. \quad (3.9)$$

Here,  $\dot{\mathbf{A}}_k$  is the  $k$ -th column of  $\dot{\mathbf{A}}$ . Sparse regression, such as the LASSO (Tibshirani 1996) or the sequential thresholded least-squares algorithm used in SINDy, improves the numerical robustness of this identification for noisy overdetermined problems, in contrast to earlier methods (Wang *et al.* 2011) that used compressed sensing (Donoho 2006; Candès 2006). Once identified, the sparse vectors  $\Xi_k$  may be synthesized into a nonlinear dynamical system model:

$$\frac{da_k}{dt} = \Theta(\mathbf{a})\Xi_k, \quad (3.10)$$

where  $a_k$  is the  $k$ -th element of  $\mathbf{a}$  and  $\Theta(\mathbf{a})$  is a row vector of symbolic functions of  $\mathbf{a}$ , as opposed to the data matrix  $\Theta(\mathbf{A})$ . Identifying the most parsimonious nonlinear model by applying sparse regression in the library  $\Theta$  is a convex procedure. The

alternative approach, which involves regression onto every possible sparse nonlinear structure, constitutes an intractable brute-force procedure. SINDy thus bypasses this combinatorial search with modern convex optimization and machine learning. The SINDy algorithm is closely related to NARMAX models (Billings 2013) and fast function extraction (FFX) (McConaghy 2011).

A major benefit of the SINDy architecture is its ability to identify parsimonious models that contain only the required nonlinear terms, resulting in interpretable models that avoid overfitting. In the optimization above, the sparsifying parameter  $\lambda$  may be varied from  $\lambda = 0$  (i.e., least-squares) to  $\lambda \rightarrow \infty$  (i.e., trivial dynamics  $d\mathbf{a}/dt = \mathbf{0}$ ), sweeping out a Pareto front. To identify the most parsimonious model that best balances model complexity with accuracy, Mangan *et al.* (2017) proposed an efficient methodology to rank candidate models on the Pareto front using the Akaike information criterion (AIC) (Akaike 1974) or the Bayes information criterion (BIC) (Schwarz *et al.* 1978).

The embedding of nonlinear dynamics in terms of a linear regression problem in (3.9) makes the SINDy method highly extensible. Recent extensions to SINDy enable the identification of nonlinear differential equations with rational function nonlinearities by reformulating the problem as an implicit differential equation and solving for the active terms by finding the sparsest vector in the null space of an augmented library containing functions of the state and derivative terms (Mangan *et al.* 2016). SINDy has also been generalized to identify partial differential equations from data (Rudy *et al.* 2017; Schaeffer 2017), and has been extended to include inputs and control (Brunton *et al.* 2016c).

### 3.3. Full-state estimation

The proposed methodology enables the identification of a low-order model that reproduces the system dynamics recorded by a few sensors. Although it may provide useful insights into the physics, it does not allow for a straightforward full-state estimation of the system considered. To accommodate this estimation, one needs to define a function

$$\mathbf{h}(\mathbf{x}, \mathbf{a}) \approx \mathbf{u}(\mathbf{x}, t) \quad (3.11)$$

mapping the state of the system from the low-dimensional feature space to the high-dimensional physical space. In the most general case,  $\mathbf{h}$  is a nonlinear mapping function. Note however that  $\mathbf{h}(\mathbf{x}, \mathbf{0})$  physically corresponds to the reference state  $\mathbf{u}_s(\mathbf{x})$  at  $\mathbf{a} = \mathbf{0}$ . While this reference state is classically chosen as the mean flow, in the present work, it is chosen as the linearly unstable steady solution  $\mathbf{u}_s(\mathbf{x})$  of the Navier-Stokes equations. In the following, two different strategies to approximate  $\mathbf{h}(\mathbf{x}, \mathbf{a})$  from data will be presented.

#### 3.3.1. Local linear mapping

Let us consider, for the sake of simplicity and without loss of generality, the feature vector  $\mathbf{a} = [a_1 \ a_2]^T$ . Given different transient evolutions of  $\mathbf{a}(t)$ , and having stored the associated velocity field snapshots, the nonlinear mapping  $\mathbf{h}(\mathbf{x}, \mathbf{a}) \approx \mathbf{u}(\mathbf{x}, t)$  can be approximated by a local linear mapping. In the rest of this work,  $\mathbf{a}^\bullet(t)$  will denote time-evolutions of the feature vector obtained from a direct numerical simulation, while  $\mathbf{a}^\circ(t)$  will denote the evolution predicted by the low-dimensional models identified using the SINDy architecture outlined in §3.2. A Delaunay triangulation of the phase plane of the low-dimensional system can then be obtained from the transient evolutions of  $\mathbf{a}_1^\bullet(t)$  and  $\mathbf{a}_2^\bullet(t)$  in the training dataset. An example triangulation is illustrated in figure 4(a). Estimating the flow field associated with a point  $[a_1^\circ \ a_2^\circ]$  then amounts to a two-step procedure:

- (i) Given the Delaunay triangulation of the phase plane, identify in which triangle the point  $[a_1^\circ \ a_2^\circ]$  is contained. See figure 4 for an illustration.

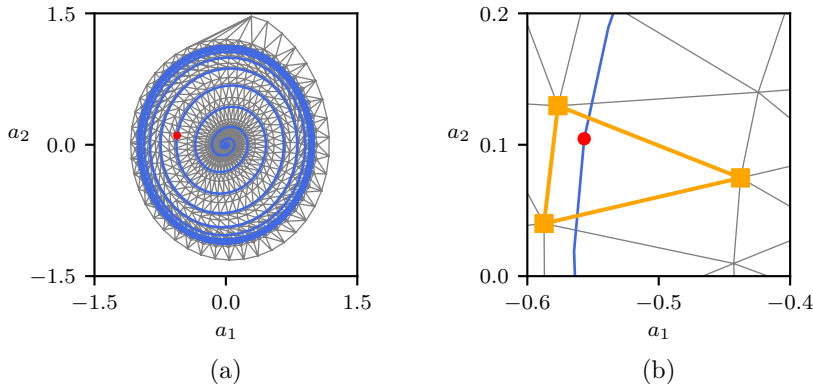


FIGURE 4. In both figures, the blue line depicts the trajectory of the testing dataset for which we reconstruct the flow field. (a) Delaunay triangulation of the state plane. In addition to the two transient trajectories started from the fixed point, a third trajectory with an initial condition above the limit cycle has been used to obtain this triangulation. (b) Close-up view in the vicinity of the query point (•). The corresponding flow field can then be estimated as a weighted average of the flow fields associated to each vertex of the triangle highlighted in green.

(ii) Based on the vertices of this triangle, the flow field associated to  $[a_1^\circ \ a_2^\circ]$  can then be estimated as a weighted average of the flow fields associated to each vertex. In the present work, these weights are chosen such that the query point  $[a_1^\circ \ a_2^\circ]$  is the barycentre of the corresponding triangle.

Although it may be memory-intensive, since numerous snapshots need to be stored, it will be shown in §4.2 that this local linear mapping procedure allows for an unprecedented accuracy when reconstructing the flow field given only sensor measurements. Further, it is possible to reduce the memory by compressing the snapshots.

### 3.3.2. Feature-based modal expansion

If full-state snapshots of the flow field are available, then it is possible to construct a set of generalized feature-based modes that are most correlated with either the feature vector  $\mathbf{a}$  or with specific nonlinear terms in the sparse model (3.4). These feature-based modes make the sparse models physically interpretable, providing spatial structures associated with feature variables and specific interaction terms in the dynamics.

Consider a sequence of full-state snapshots<sup>‡</sup>

$$\mathbf{Q}(\mathbf{x}) = [\mathbf{u}^{m_1}(\mathbf{x}) \ \mathbf{u}^{m_2}(\mathbf{x}) \ \mathbf{u}^{m_p}(\mathbf{x})]. \quad (3.12)$$

Note that these snapshots do not need to be time-resolved, but they are collected at times  $t^{m_1}, \dots, t^{m_p}$  that correspond to a subset of the resolved measurement times with which  $\mathbf{s}$  and  $\mathbf{a}$  are collected. Recall that the columns of  $\mathbf{A}^T$  are a time-resolved sequence of feature vectors  $\mathbf{a}(t^m)$ , with  $m = 1, \dots, M$ . The columns of  $\mathbf{A}^T$  associated with the non-time-resolved snapshots in  $\mathbf{Q}$  are given by

$$\mathbf{A}_Q^T = [\mathbf{a}(t^{m_1}) \ \mathbf{a}(t^{m_2}) \ \dots \ \mathbf{a}(t^{m_p})]. \quad (3.13)$$

<sup>‡</sup> Note that the columns of the matrix  $\mathbf{Q}$  correspond to a time-sequence of full-state snapshots, which is the mathematical convention in snapshot proper orthogonal decomposition and dynamic mode decomposition (Kutz *et al.* 2016). However, the matrix  $\mathbf{A}$  uses transposed notation to be consistent with the original SINDy paper (Brunton *et al.* 2016b), with rows corresponding to a time-sequence of transposed feature vectors  $\mathbf{a}^T$ . Thus, the columns of  $\mathbf{A}^T$  are a time-sequence of the features  $\mathbf{a}$ , similar to  $\mathbf{Q}$ .

Thus, the snapshots sequence may be approximated by

$$\mathbf{Q} = \mathbf{U}(\mathbf{x})\mathbf{A}_Q^T(t) + \mathbf{R}(\mathbf{x}, t), \quad (3.14)$$

where  $\mathbf{R}$  is the truncation residual. The columns of  $\mathbf{U}(\mathbf{x})$  are feature-based modes that are most correlated with the terms in the feature vector  $\mathbf{a}(t)$ . These modes are found via least-squares regression:

$$\mathbf{U} = \mathbf{Q} (\mathbf{A}_Q^T)^\dagger, \quad (3.15)$$

where  $(\mathbf{A}_Q^T)^\dagger$  is the Moore-Penrose pseudo-inverse of  $\mathbf{A}_Q^T$ . In practice, this least-squares regression may be solved efficiently using the singular value decomposition of  $\mathbf{A}_Q^T$ .

More generally, it is possible to compute modes that are most correlated with the dynamic interaction terms in the sparse model (3.8). Let  $\gamma_1, \dots, \gamma_q$  denote the indices of the rows in  $\Xi$  with non-zero entries, i.e. corresponding to active terms in the sparse dynamics. The corresponding terms in the dynamics may be extracted via:

$$\boldsymbol{\alpha} = (\Theta(\mathbf{a}) [\mathbf{e}_{\gamma_1} \quad \mathbf{e}_{\gamma_2} \quad \dots \quad \mathbf{e}_{\gamma_q}])^T, \quad (3.16)$$

where  $\mathbf{e}_{\gamma_j}$  is a column vector consisting entirely of zeros, except for a one in the  $\gamma_j$ -th row; i.e.,  $\mathbf{e}_{\gamma_j}$  is the  $\gamma_j$ -th column of the identity matrix. For example, in the results, we will consider a vector of nonlinear terms  $\boldsymbol{\alpha}$  given by  $\boldsymbol{\alpha} = [a_1 \quad a_2 \quad a_1^2 + a_2^2 \quad 2a_1a_2 \quad a_1^2 - a_2^2]^T$ . It is now possible to obtain generalized modes:

$$\mathbf{U} = \mathbf{Q} ([\boldsymbol{\alpha}(t^{m_1}) \quad \boldsymbol{\alpha}(t^{m_2}) \quad \dots \quad \boldsymbol{\alpha}(t^{m_p})])^\dagger. \quad (3.17)$$

Thus, each mode  $\mathbf{u}_i(\mathbf{x})$  is a spatial field corresponding to a specific interaction term in the dynamical system, given by a component of  $\boldsymbol{\alpha}$ .

Compared to the local linear mapping presented in §3.3.1, such a feature-based expansion has a low memory footprint, although it will typically be less accurate. However, even if the feature-based modes are not used for full-state reconstruction, they imbue the sparse model with physical interpretability. The modal representation above may be thought of as closely related to the proper orthogonal decomposition or dynamic mode decomposition, except generalized to identify modes that are most correlated with the features in  $\mathbf{a}$  or the dynamic interaction terms in  $\boldsymbol{\alpha}$ .

## 4. Results

### 4.1. Sensor-based dynamics

In this section, a low-dimensional model of the transient and post-transient laminar cylinder wake is presented. First, a dynamical model capturing the dynamics of the lift coefficient is identified in §4.1.1. Then, in §4.1.2, the low-order model aforementioned is supplemented with a nonlinear algebraic measurement equation in order to infer the evolution of the drag coefficient.

#### 4.1.1. Dynamical system

It is well known that the two-dimensional cylinder flow behaves as a self-excited, self-limiting and nearly harmonic nonlinear oscillator. This behavior is clearly visible in the time-evolution of the instantaneous lift coefficient depicted in figure 2. As such, the dynamics can be described by a nonlinear second-order ordinary differential equation, or by a set of two coupled first-order ODEs. Given our feature vector  $\mathbf{a}$  (3.3), mapping the state of the system from the sensor-space to the feature-space, is defined as

$$\mathbf{a} = [\hat{a}_1 \quad \hat{a}_2]^T, \quad (4.1)$$

with  $\hat{a} = \frac{a}{a_{\max}}$ ,  $a_{\max}$  being the maximum value of  $a$  once the system evolves onto the periodic limit cycle. Such normalization ensures that

$$-1 \leq a_{1,2} \leq 1,$$

a condition which greatly simplifies the sparse optimization problem involved in the identification procedure. Although this mapping function has been defined analytically in the present work, similar features could be identified using delay coordinates, as in the singular spectrum analysis (SSA) in meteorology and ecology (Colebrook 1978; Barnett & Hasselmann 1979; Weare & Nasstrom 1982; Ghil *et al.* 2002), NARMAX (Billings 2013), the eigensystem realization algorithm (ERA) from system identification and control theory (Juang & Pappa 1985); these delay coordinates have recently been connected to the linear embedding of nonlinear dynamics via Koopman operator theory (Brunton *et al.* 2017; Arbabi & Mezić 2016). Alternatively, one could have also used the Hilbert transform for that purpose.

Based on the different transient time evolutions of  $\mathbf{s}^\bullet(t)$  recorded from direct numerical simulations, the corresponding feature vectors  $\mathbf{a}^\bullet(t)$  have been computed and grouped into our training dataset. The *Sparse Identification of Nonlinear Dynamics* (Brunton *et al.* 2016b), briefly outlined in §3.2, is used to identify the equations governing the dynamics of  $\mathbf{a}$ . The pool of candidate functions required for the identification process is chosen as

$$\Theta(a_1, a_2) = [1 \quad a_1 \quad a_2 \quad a_1^2 \quad a_1 a_2 \quad a_2^2 \quad a_1^3 \quad a_1^2 a_2 \quad a_1 a_2^2 \quad a_2^3]. \quad (4.2)$$

Such a pool of polynomial functions, which can easily be enriched if needed, is a natural choice for the identification of a nonlinear oscillator (Holmes & Guckenheimer 1983). In the present case, it leads to the identification of the following dynamical system

$$\frac{d}{dt} \begin{bmatrix} a_1 \\ a_2 \end{bmatrix} = \begin{bmatrix} 0 & 1.12 \\ -1.116 & 0.28(1 - a_1^2 - a_2^2) \end{bmatrix} \begin{bmatrix} a_1 \\ a_2 \end{bmatrix}. \quad (4.3)$$

More details about the model selection procedure can be found in appendix A. As shown in figure 5, the time evolution of  $a_1^\circ(t)$  predicted by this low-dimensional system is in very good agreement with the one obtained for  $a_1^\bullet(t)$  based on a direct numerical simulation whose initial condition has been chosen in the vicinity of the linearly unstable baseflow. It is also remarkable that, despite its apparent simplicity, this two-degrees-of-freedom system captures all of the key physics of the cylinder flow, namely:

- It admits only one linearly unstable fixed point given by  $\mathbf{a} = \mathbf{0}$  and one attracting limit cycle characterized by  $\|\mathbf{a}\| = 1$ . The corresponding circular frequency  $\omega^\circ = 1.119$  in the nonlinearly saturated state is moreover less than 1.5% smaller than the one observed in DNS ( $\omega^\bullet = 1.132$ ).
- It explicitly highlights the quadratic dependency of the instantaneous growth rate  $2\sigma(\mathbf{a}) = 0.28(1 - a_1^2 - a_2^2)$ . Such quadratic dependencies are in line with our current understanding of the nonlinear saturation process of globally unstable flows; see Mantić-Lugo *et al.* (2014) for more details.
- Once the amplitude of the oscillation has saturated to  $\|\mathbf{a}\| = 1$ , the system reduces to a simple harmonic oscillator. A similar structure could be derived based on a Galerkin projection of the Navier-Stokes equations onto the span of the first two POD modes and using the marginally stable mean flow as the reference state.

From a physical point of view, this low-order system describes the dynamics of the original high-dimensional system when constrained to the low-dimensional manifold structuring its phase phase (Noack *et al.* 2003).

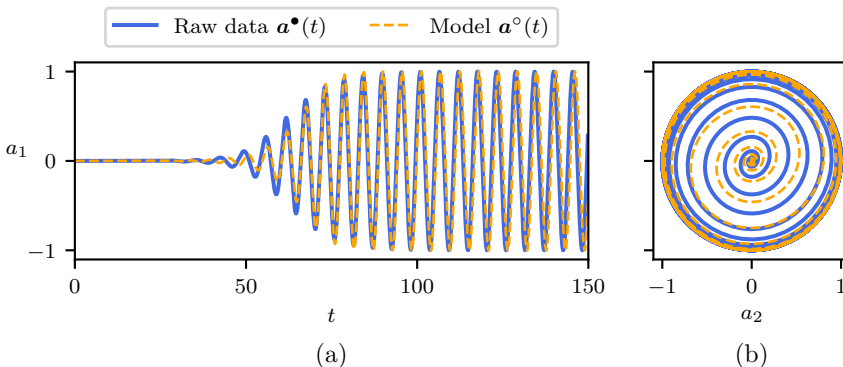


FIGURE 5. (a) Comparison of the evolution as a function of time of the sensor measurement  $a_1$  obtained from direct numerical simulation (—  $a_1^\bullet(t)$ ) and predicted by the identified low-dimensional model (4.3) (---  $a_1^\circ(t)$ ). (b) Trajectory of the true and identified systems in the phase plane  $(a_1, a_2)$ . In both cases, the initial condition is close to the linearly unstable fixed point  $\mathbf{u}_b(\mathbf{x})$ , given by  $\mathbf{a} = \mathbf{0}$ .

Although the particular transient evolution of  $a_1^\bullet(t)$  depicted in figure 5 has not been included in the training dataset, it is nonetheless characteristic of the type of evolution that our model has been specifically trained on. One might then wonder how the model generalizes, for instance, given an initial condition that lies outside of the limit cycle. Such an evolution is shown in figure 6 for an initial condition that has a radius from the fixed point that is 33% larger than the radius of the limit cycle. Note that, for physical reasons, the initial condition used in the direct numerical simulation has been chosen such that it is close to the low-dimensional inertial manifold. Once again, the dynamics of  $a_1^\circ(t)$  predicted by (4.3) are in qualitative and quantitative agreements with the actual dynamics of  $a_1^\bullet(t)$  obtained from the corresponding direct numerical simulation. Finally, it is worth noting that, although we have aimed for a continuous-time representation of the dynamics in this work, the present methodology can easily be adapted to obtain a discrete-time version of the same system, as described in appendix B.

#### 4.1.2. Descriptor system

The dynamical system identified in §4.1 provides valuable information and accurate predictions of the dynamics of the system. However, being based solely on quantities derived from the instantaneous lift coefficient, the model does not enable direct estimation of the corresponding drag force. Having a model that can estimate the instantaneous drag force might, however, be of critical importance in aerodynamic applications. Defining the drag coefficient as a degree of freedom of our system, two different possibilities are then available: (i) extend the dynamical system (4.3) with a (nonlinear) algebraic measurement equation, or (ii) identify a new dynamical system made of three coupled ODEs. We have investigated both of these options, and found that models may be successfully identified. Given the simplicity and accuracy of the dynamical system (4.3) identified in §4.1.1, the former approach is preferred over the latter. For that purpose, an additional feature is added to  $\mathbf{a}$ , given by

$$a_3(t) = \frac{C_D(t) - C_{D_0}}{\max(C_D(t) - C_{D_0})},$$

where  $C_{D_0}$  denotes the instantaneous drag coefficient of the base flow  $\mathbf{u}_s(\mathbf{x})$ , and  $\max(C_D(t) - C_{D_0})$  is the maximum value once the flow has reached its statistically

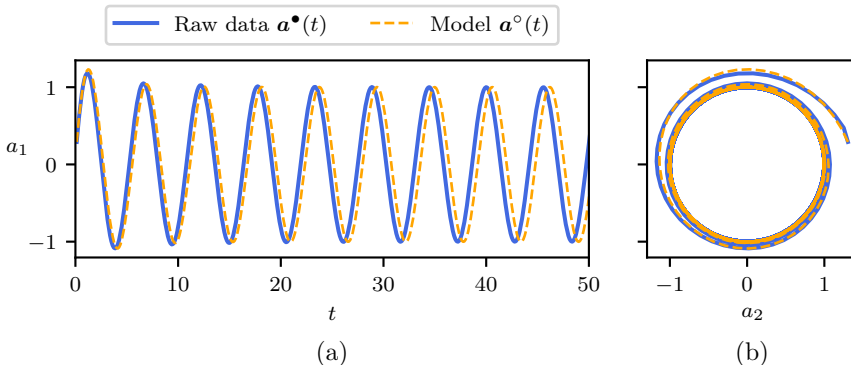


FIGURE 6. (a) Comparison of the evolution as a function of time of the sensor measurement  $a_1$  obtained from direct numerical simulation (—  $a_1^\bullet$ ) and predicted by the identified low-dimensional model (4.3) (---  $a_1^\circ$ ). (b) Trajectory of the true and identified systems in the phase plane  $(a_1, a_2)$ . The initial condition used in the direct numerical simulation has been chosen to lie outside of the limit cycle, and for physical reasons it is also constrained to start close to the paraboloid manifold structuring the phase space of the system.

stationary state. We thus seek a nonlinear algebraic measurement equation of the form

$$a_3 = f(a_1, a_2).$$

This algebraic measurement equation can also be identified using sparse regression with the same pool  $\Theta(a_1, a_2)$  of candidate functions (4.2) as before. Given our training dataset, the parsimonious measurement equation identified reads

$$a_3^2 = 0.97a_1^2 - 0.16a_1a_2 + 0.84a_2^2. \quad (4.4)$$

Combining this measurement equation with the dynamical system (4.3) identified in §4.1.1 results in a low-dimensional descriptor system governing the evolution of both the instantaneous lift and drag coefficients.

Equation (4.4) describes a distorted cone and is notably different from the mean-field paraboloid of the 3-dimensional POD-Galerkin model by Noack *et al.* (2003). This difference can be explained by the choice of the state space  $\mathbf{a}$ . The oscillation of von Kármán vortex shedding is characterized by  $a_1$  and  $a_2$ —albeit from different physical mechanisms. During the transient, the vortex shedding moves upstream from the stagnation point of the unstable steady solution to the immediate vicinity of the cylinder. The global POD mode amplitudes  $a_1, a_2$  resolve the vortex shedding already far downstream, while the lift-based feature coordinates ‘feel’ the vortex shedding only in the final stage when the vortices ‘rub’ on the cylinder. In contrast, the drag variation and the shift-mode amplitude of the 3-dimensional POD-Galerkin model are linearly related. Thus,  $a_3$  of the Galerkin expansion and of the force-related ROM resolve the same physics. Hence, the fluctuation amplitude  $\sqrt{a_1^2 + a_2^2}$  increases much faster with  $a_3$  for the POD-based model than for the force-based system.

Figure 7(a) and figure 8(a) compare the predicted time-evolution of  $a_3^\circ(t)$  against the evolution of  $a_3^\bullet(t)$  obtained from direct numerical simulation, whereas figure 7(b) and figure 8(b) depict the associated trajectories projected onto the  $(a_1, a_3)$  phase plane. Along with the dynamics of  $a_1$  and  $a_2$  being correctly captured by the dynamical system (4.3), it is clear that the nonlinear algebraic measurement equation (4.4) correctly infers the evolution of  $a_3$ . Although a small misprediction of the amplitude of  $a_3$  can be seen for  $45 \leq t \leq 65$ , the low-dimensional descriptor system identified in the present work

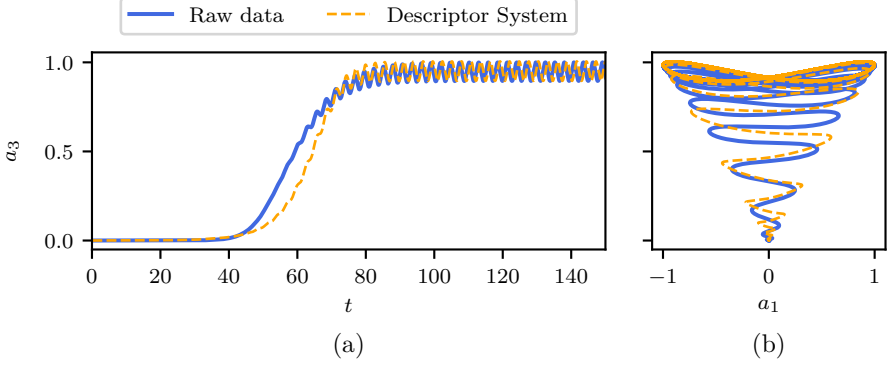


FIGURE 7. (a) Comparison of the evolution as a function of time of the sensor measurement  $a_3$  obtained from direct numerical simulation (—  $a_3^\bullet$ ) and predicted by the identified low-dimensional descriptor system made of (4.3) and (4.4) (---  $a_3^\circ$ ). (b) Trajectory of the true system and the identified one in the phase plane  $(a_1, a_3)$ .

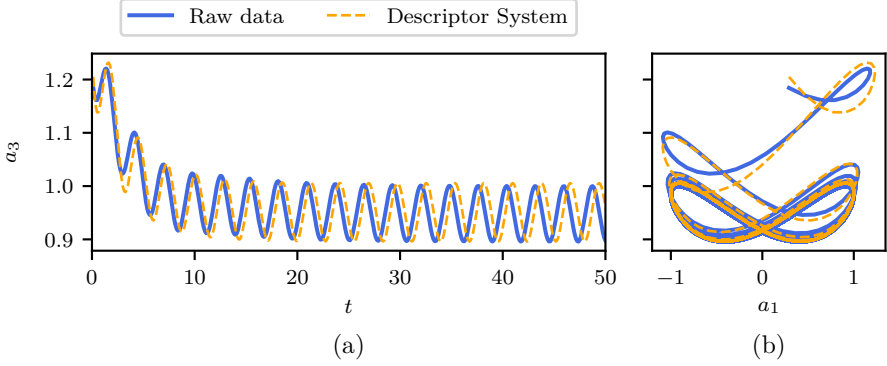


FIGURE 8. (a) Comparison of the evolution as a function of time of the sensor measurement  $a_3$  obtained from direct numerical simulation (—  $a_3^\bullet$ ) and predicted by the identified low-dimensional descriptor system made of (4.3) and (4.4) (---  $a_3^\circ$ ). (b) Trajectory of the true system and the identified one in the phase plane  $(a_1, a_3)$ .

is nonetheless one of the simplest and yet most accurate and physically interpretable low-order models available in the literature to reproduce the dynamics of the cylinder flow at  $Re = 100$ .

#### 4.2. Flow field estimation

The descriptor system identified in the previous section provides valuable information and accurate predictions of the dynamics of the system. However, it does not allow us to directly infer what the corresponding flow field is. In order to estimate the flow, we thus need to supplement our dynamical system with a full-state estimator given by

$$\mathbf{u}(\mathbf{x}, t) \approx \mathbf{h}(\mathbf{x}, \mathbf{a}(t)).$$

Formally, this full-state estimator  $\mathbf{h}$  is a nonlinear mapping from the low-dimensional feature-space to the high-dimensional physical space. In the rest of this section, two different strategies will be employed in order to build this nonlinear mapping: the local



linear mapping procedure described in §3.3, or a feature-based modal expansion of the velocity field in terms of the feature modes introduced in §3.3.2.

Given a sparse nonlinear model, it is also possible to construct a generalized feature-based modal decomposition that identifies modal structures that are most correlated with specific terms in the dynamics. We define a new feature vector  $\alpha$  containing all of the nonzero terms identified in the right hand side of the sparse model:

$$\alpha \triangleq \begin{bmatrix} a_1 \\ a_2 \\ a_1^2 + a_2^2 \\ 2a_1 a_2 \\ a_1^2 - a_2^2 \end{bmatrix} = \begin{bmatrix} \alpha_1 \\ \alpha_2 \\ \alpha_3 \\ \alpha_4 \\ \alpha_5 \end{bmatrix}. \quad (4.5)$$

The feature-based modal expansion considered hereafter then reads

$$\mathbf{u}(\mathbf{x}, t) = \mathbf{u}_0(\mathbf{x}) + \sum_{i=1}^5 \mathbf{u}_i(\mathbf{x}) \alpha_i(t) + \mathbf{r}(\mathbf{x}, t) \quad (4.6)$$

where  $\mathbf{u}_0(\mathbf{x})$  is the linearly unstable steady solution to the Navier-Stokes equations and  $\mathbf{r}(\mathbf{x}, t)$  the residual. The different feature modes  $\mathbf{u}_i(\mathbf{x})$  have been computed following the procedure described in §3.3. Mathematically, the generalized mode decomposition is achieved with a simple least-squares regression:

$$\mathbf{Q} \approx \underbrace{\begin{bmatrix} | & | & | & | & | \\ \mathbf{u}_1(\mathbf{x}) & \mathbf{u}_2(\mathbf{x}) & \mathbf{u}_3(\mathbf{x}) & \mathbf{u}_4(\mathbf{x}) & \mathbf{u}_5(\mathbf{x}) \\ | & | & | & | & | \end{bmatrix}}_{\text{Modes: } \mathbf{U}} \underbrace{\begin{bmatrix} \text{---} \alpha_1(t) \text{---} \\ \text{---} \alpha_2(t) \text{---} \\ \text{---} \alpha_3(t) \text{---} \\ \text{---} \alpha_4(t) \text{---} \\ \text{---} \alpha_5(t) \text{---} \end{bmatrix}}_{\text{Time dynamics: } \alpha(t)} \Rightarrow \mathbf{U} = \mathbf{Q} (\alpha(t))^\dagger \quad (4.7)$$

where  $(\alpha(t))^\dagger$  denotes the pseudo-inverse of the matrix  $\alpha(t)$ , and  $\mathbf{Q}$  is the sequence of baseflow-subtracted snapshots.

The associated vorticity fields are shown in figure 10, while the time-evolution of the different basis coefficients  $\alpha_i(t)$  is depicted in figure 9(a). Figure 9(b) shows the cross correlation matrix of these signals. Given its diagonal structure, it is clear that the different basis coefficients  $\alpha_i(t)$  are uncorrelated one to another. For the cylinder flow, these feature modes are very similar to the classical POD modes. A key advantage over POD modes is that the present modes are directly interpretable as being the coherent structures most correlated with our different measurements and the sparse nonlinear interaction terms in the model. Moreover, the shift mode  $\mathbf{u}_3$  naturally arises in this framework as the result of quadratic interactions between  $a_1$  and  $a_2$ , consistent with our understanding of the nonlinear saturation of globally unstable flows (Mantić-Lugo *et al.* 2014). Defining the feature vector  $\alpha$  used in the feature-based modal expansion such that it includes quadratic terms was thus deemed necessary in order to ensure that the distortion between the linearly unstable base flow and the marginally stable mean flow is correctly captured by the flow estimator using the feature-based modal expansion (4.6).

Figure 11 compares the evolution of  $\|\mathbf{r}\|$ , i.e. the norm of the estimation error, for the local linear mapping and the feature-based modal expansion (4.6). The evolution of the truncation error for different POD bases is also reported for the sake of comparison. The flow estimator based on the local linear mapping (LLM) largely outperforms the two estimators based on a 5-mode POD expansion and the generalized modal decomposition

with 5 modes. Its very good performances, on average two to three orders of magnitude more accurate than the other estimators considered, results from the fact that LLM leverages all of the information contained in the different snapshots matrices used whereas the different modal expansions only provide low-rank approximations of these same matrices. However, this higher accuracy comes at the price of increased storage. This requirement can nonetheless be mitigated by computing a low-rank approximation of the snapshot matrix used in the training dataset. In the present case, considering a rank-50 approximation based on the singular value decomposition has almost no effect on the estimation error, while significantly reducing the memory requirements. Instead of storing  $M = 1,200$  snapshots, each a 100,000-dimensional vector corresponding to a vertex of the Delaunay triangulation of phase space, only the 50 leading full-state singular vectors must be stored, along with the 50-dimensional vector of coefficients for each vertex. This reduces the storage requirements by a factor of nearly 24. In this case, the local linear mapping would then approximate the transfer function mapping the state of our system from the 2-dimensional phase space of the dynamical system (4.3) to the 50-dimensional space of coefficients resulting from the truncated singular value decomposition of the snapshots matrix.

Finally, figures 12(b) and (c) depict the estimated vorticity field, with the base flow subtracted, at different instants in time and compare them with the true vorticity field obtained from direct numerical simulation in figure 12(a). The vorticity fields estimated using the local linear mapping are in much better agreement, from a physical and kinematic point of view, than the ones obtained by the 5-mode modal expansion. This is especially pronounced during the period of exponential growth of the linear instability and at the onset of nonlinear saturation during which the local linear mapping correctly captures the deformation and distortion of the flow structure. In contrast, low-rank modal expansions are notorious for their inability to capture such mode deformation and/or changes in operating conditions. Given that the POD modes and generalized feature modes used in this work essentially approximate the flow structure once the system has reached the periodic limit cycle, it is thus expected that they provide only a very crude estimation of the flow structures when the system evolves in the vicinity of the linearly unstable base flow. This inability of a modal expansion to easily address mode deformation is one of its key limitations and is the principal reason why the local linear mapping strategy should be preferred. Combining the descriptor system identified in §4.1 with the local linear flow estimator finally allows us to construct a two-degrees-of-freedom reduced-order model of the cylinder flow, having an unprecedented accuracy.

## 5. Conclusions

This work develops a new reduced-order modeling procedure for unsteady fluid flows that yields accurate nonlinear models and insight into relevant flow structures. This procedure identifies sparse nonlinear models, not on the full fluid state, but from time-resolved sensor measurements that may be realistically obtained in experiments. The sparsity of the model prevents overfitting and uncovers key nonlinear interaction terms. If PIV snapshots are also available, not necessarily time-resolved, it is possible to estimate the full-state from the sparse model using local linear mapping: the full-state is interpolated between the most similar historical flow fields, based on the dynamics. It is also possible to construct a generalized modal decomposition that identifies coherent structures most correlated with each interaction term in the sparse nonlinear model.

Our methodology, summarized in figure 1, can be divided into four steps:

- (i) Given a set of physically relevant sensor measurements  $\mathbf{s}$ , create a low-dimensional

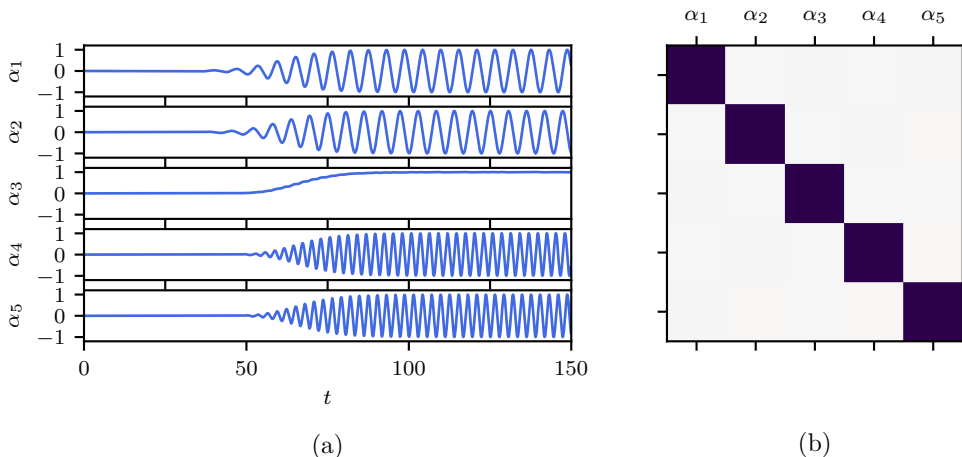


FIGURE 9. (a) Time evolution of the different basis coefficients used in the feature-based modal expansion (4.6). (b) Corresponding cross-correlation matrix. Dark squares indicate that  $\alpha_i$  and  $\alpha_j$  are strongly correlated, while white squares indicate they are uncorrelated.

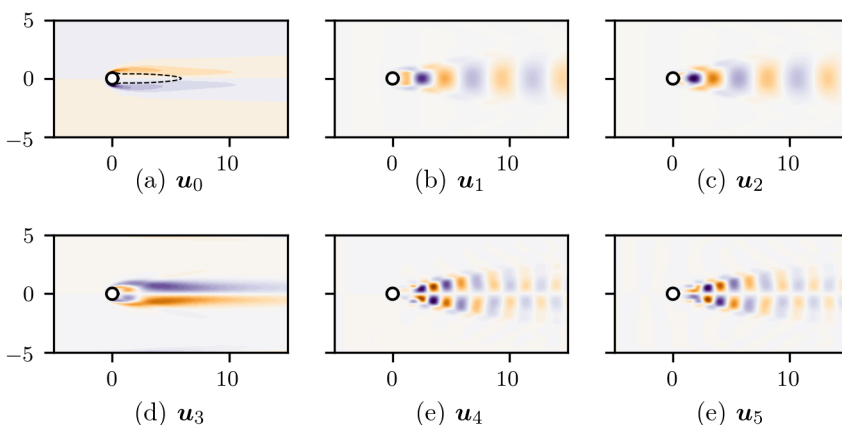


FIGURE 10. Figure (a) depicts the vorticity field of the linearly unstable base flow, while the dashed line highlights the spatial extent of the reversed flow region. Figures (b) to (e) show the vorticity field of the feature modes associated to the feature vector  $\mathbf{b}$ .

feature vector  $\mathbf{a}$  that allows for a complete dynamics characterization of the state of the system. Although we have used an analytical mapping  $\mathbf{a} = \mathbf{g}(\mathbf{s})$  in the present work, this procedure could also be performed, for instance, by means of kernel PCA (Schölkopf *et al.* 1998). Moreover, the sensors could come from force measurements, as in the present work, or from any other time resolved sensor measurements, such as pressure along the body. In the case of limited measurements, it may also be possible to augment the state using delay coordinates (Takens 1981), in the spirit of SSA (Colebrook 1978; Barnett & Hasselmann 1979), NARMAX (Billings 2013), ERA (Juang & Pappa 1985), or HAVOK (Brunton *et al.* 2017) models; delay coordinates have since been connected to Koopman operator theory (Brunton *et al.* 2017; Arbabi & Mezić 2016).

(ii) The second step identifies the equations governing the dynamics of  $\mathbf{a}$ . In this study, the SINDy algorithm (Brunton *et al.* 2016b) yields a sparse nonlinear model in

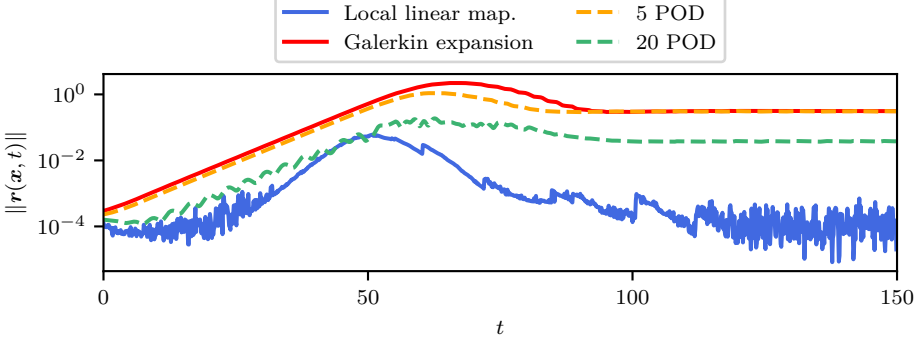


FIGURE 11. Time evolution of the estimation error  $\|\mathbf{r}(\mathbf{x}, t)\|$  for different flow estimators.

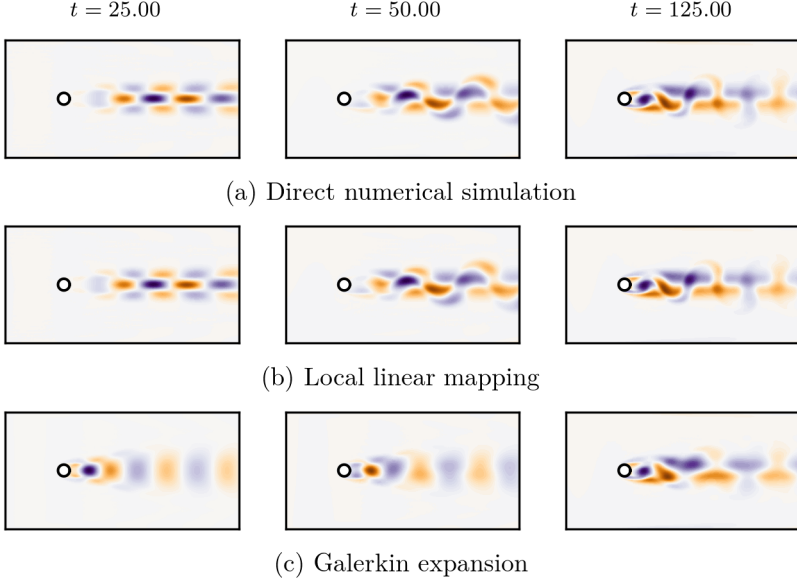


FIGURE 12. Comparison of the vorticity fields at different instants of time obtained (a) from direct numerical simulation, (b) from the local linear mapping procedure and (c) from the feature-based modal expansion. Note that the vorticity field of the linearly unstable baseflow has been subtracted in order to highlight the perturbative vorticity field.

continuous-time. Discrete-time models may also be obtained via SINDy, or using the classical NARMAX or Volterra series approaches (Semeraro *et al.* 2016). In the past, nonlinear reduced-order models have primarily been obtained with knowledge of the governing equations and with the use of high-fidelity numerical simulations, such as in the Galerkin projection procedure. The present approach is exclusively data-driven, and does not rely on prior knowledge of the governing equations, which is consistent with the modern machine learning approach. Thus, interpretable models may be obtained from experimental measurements alone.

(iii) If full-state snapshots are available, it has been shown in §3.3.1 and §4.2 that the low-order model can be supplemented with a full-state estimator  $\mathbf{u}(\mathbf{x}, t) \approx \mathbf{h}(\mathbf{x}, \mathbf{a})$ . The full-state snapshots do not need to be time-resolved, but they do need to be synchronized

with the sensor measurements. The local linear mapping procedure provides a highly accurate approximation  $\mathbf{h}(\mathbf{x}, \mathbf{a})$ . Full-state estimation is particularly relevant in control applications (Fabbiane *et al.* 2014; Brunton & Noack 2015; Sipp & Schmid 2016), where feedback control is often designed on the full state, which is then estimated from sensor measurements (Dullerud & Paganini 2000; Skogestad & Postlethwaite 2005). If the sensor measurements are noisy, it may also be helpful to design a Kalman filter (Kalman 1960; Welch & Bishop 1995) based on the sparse dynamics, so that the estimated state does not jump in response to noise jitter.

(iv) Although the local linear mapping yields the most accurate full-state reconstruction, it may also be useful to identify a generalized modal expansion for interpretability of the low-order model. Through simple regression, it is possible to identify modal structures that are most correlated with each term in the SINDy model. This procedure is similar in concept to DMD, but generalized to identify structures associated with nonlinear terms in the model. These coherent structures may improve intuition and interpretability. Some challenges and improvements of DMD for transient cylinder wakes have been described by Noack *et al.* (2016).

This methodology is illustrated using the canonical two-dimensional cylinder flow at  $Re = 100$ . Despite its simplicity, this flow configuration is a prototypical example capturing the key physics of bluff body flows. Various models are identified based on sensor measurements of the lift and drag coefficients,  $C_L$  and  $C_D$ , which are physically relevant and are readily accessible in experiments. First, a dynamical system (4.3) is identified using a single sensor input  $s = C_L$ , which is augmented with its time derivative. As discussed in §4.1.1, this system models the cylinder flow dynamics, which evolve along a low-dimensional manifold. Next, in §4.1.2, the same dynamical system may be supplemented with a sparse nonlinear equation to build an algebraic representation of the drag coefficient  $C_D$  in terms of the evolution of  $C_L$ . It is also possible to build a reduced model with three degrees of freedom in terms of  $C_L$ , its time derivative, and  $C_D$ . This model is the most general and has a broader range of validity, as it captures the low-dimensional slow-manifold structure underlying phase space. Finally, the local linear mapping in §4.2 provides full-state estimation with unprecedented accuracy compared to the classical Galerkin expansion.

Even though this study uses data from direct numerical simulations, the overall strategy is generally applicable to a real flow experiment with minor modifications. Despite their simplicity, the identified models do not suffer the same drawbacks as reduced-order models obtained from a Galerkin projection procedure, namely over-estimation of the duration of transients and energy overshoots at the onset of nonlinear saturation. Instead, the identified sparse models provide simple explanations for the nonlinear saturation process of globally unstable flows, as in (4.3). Moreover, the models are based on sensor measurements, which may include lift, drag, or pressure measurements that are physically linked to the geometry. Working in these *intrinsic* coordinates has the potential to overcome many of the limitations of classical modal-based projection methods, including mode deformation due to moving geometry and varying parameters.

The effectiveness of the reduced-order models identified and the modularity of the methodology proposed in the present work suggest a number of exciting future directions. There is significant potential for these methods to be applied broadly to obtain interpretable reduced-order models for a range of flow configurations in simulations and experiments. For example, these sensor-based models may be applied to develop nonlinear unsteady aerodynamic models, generalizing previous linear and linear parameter varying models (Brunton *et al.* 2013, 2014; Hemati *et al.* 2016).

A key perspective to be given to this work is its extension to flow control. Given a

feature vector  $\mathbf{a}$  and actuators characterized by a control law  $\mathbf{b}(t)$ , one could use SINDy with control (SINDYc) (Brunton *et al.* 2016c) in order to identify low-order models

$$\frac{d\mathbf{a}}{dt} = \mathbf{f}(\mathbf{a}, \mathbf{b})$$

that incorporate the influence of the actuation  $\mathbf{b}$  on the state  $\mathbf{a}$ . Combining such an approach with *Machine Learning Control* (Duriez *et al.* 2016) may result in interpretable models of entirely new flow behaviors and previously unobserved flow physics that are discovered through in the controlled flow. The identified models can then serve as a low-dimensional representation of the actual system in order to facilitate the computation of nonlinear optimal feedback control laws. This is an area of active research by the authors. In the near future, the authors aim to apply the methodology introduced in the present work to the optimal control of experimental flows.

Finally, there are a number of methodological extensions that may improve the performance of this sparse modeling framework. First, it will be important to demonstrate that these methods scale favorably to systems with higher-dimensional attractors; however, because the algorithms are based on simple regression and sparse optimization, they should remain computationally tractable. Next, it may be possible to reduce the memory requirements of the local linear mapping by building local modal libraries in different dynamic regimes (e.g., linear instability, saturated limit cycle, etc.). The storage requirements may further be reduced using compression techniques and sparse sampling. Finally, it may be possible to incorporate the accuracy of the generalized modal decomposition reconstruction into the cost function in the SINDy regression, so that nonlinear features are selected based on their dynamic relevance and their ability to correlate to full-state structures.

## Acknowledgments

SLB acknowledges generous funding support from the Defense Advanced Research Projects Agency (DARPA HR0011-16-C-0016) and from the Air Force Office of Scientific Research (AFOSR FA9550-13-1-0183). SLB would like to thank Nathan Kutz, Josh Proctor, Niall Mangan, and Sam Rudy for discussions related to sparse model identification. SLB would also like to thank Scott Dawson for valuable discussions related to nonlinear modeling in terms of aerodynamic force coefficients.

BRN acknowledges the funding and excellent working conditions of the Collaborative Research Center (CRC880) 'Fundamentals of High Lift for Future Civil Aircraft' funded by the German Science Foundation (DFG) and hosted by the Technical University of Braunschweig, Germany. This work is also supported by internal funds of LIMSI-CNRS and a public grant overseen by the French National Research Agency (ANR) as part of the "Investissement d'Avenir" program, through the "iCODE Institute project" funded by the IDEX Paris-Saclay, ANR-11-IDEX-0003-02.

## Appendix A. Model Selection

Model selection and cross-validation are crucial components of system identification, as regression models tend to overfit with increasing training data, unless care is taken. The goal is to identify, among all candidate models, the parsimonious model that optimally balances model accuracy and model complexity. As the sparsifying parameter  $\lambda$  is varied in the SINDy procedure, a Pareto front is swept out, reducing the combinatorially many candidate models down to a small handful of candidates models. Mangan *et al.*

(2017) have recently demonstrated how SINDy can be combined with the well-known Akaike information criterion (AIC) (Akaike 1974) or the Bayes information criterion (BIC) (Schwarz *et al.* 1978) in order to select the most parsimonious model from this Pareto front. Given a candidate model, the associated AIC score is given by

$$AIC = 2k - 2\ln(L(\mathbf{a}, \mu)) + 2\frac{(k+1)(k+2)}{(m-k-2)}, \quad (\text{A } 1)$$

where  $L(\mathbf{a}, \mu)$  is the loss function of the observations  $\mathbf{a}$  given the best-fit parameters values  $\mu$  of the candidate model and  $k$  the total number of free parameters. The last term in (A 1) is a finite sample size correction where  $m$  is the total number of observations used to cross-validate the model. For two models of the same accuracy, the AIC score will penalize the one having the larger number of free parameters. In this work, the loss function has been chosen as

$$L(\mathbf{a}, \mu) = \frac{1}{m} \sum \frac{\int_0^T \|\mathbf{a}^\circ(t) - \mathbf{a}^\bullet(t)\|^2 dt}{\int_0^T \|\mathbf{a}^\bullet(t)\|^2 dt} \quad (\text{A } 2)$$

where  $\mathbf{a}^\bullet(t)$  is the time-evolution obtained from direct numerical simulation of the Navier-Stokes equations and  $\mathbf{a}^\circ(t)$  is the evolution predicted by the low-dimensional model considered. The summation is over the  $m$  different training and testing datasets used for cross-validation. The AIC scores for each candidate model can have a wide range of values, hence requiring a rescaling by the minimum AIC value. The relative AIC score is thus given by

$$\Delta = AIC - AIC_{\min}. \quad (\text{A } 3)$$

The different candidate models can then be ranked based on this relative AIC score. Following Mangan *et al.* (2017), models with  $\Delta \leq 2$  have so-called *strong support*, models with  $4 \leq \Delta \leq 7$  have *weak support*, and models with  $\Delta \geq 10$  have *no support*. It should be emphasized that the model characterized by  $\Delta = 0$  is not necessarily the best model possible, but only the best one among the different models tested.

Given a library of functions,  $\Theta(a_1, a_2)$ , that includes all polynomials in  $a_1$  and  $a_2$  up to the 7<sup>th</sup> degree, figure 13 depicts the relative AIC ranking as a function of the model complexity for all of the models identified by SINDy using different sparsity values  $\lambda$  to sweep out a Pareto front. Note that, as a starting point, no constraint had been added in the identification step, and the corresponding models are given by the blue dots in figure 13. Under these conditions, the model that optimally balances accuracy and complexity has only 4 terms (blue dot in the lower panel of figure 13) and is given by

$$\begin{aligned} \frac{da_1}{dt} &= 1.12a_2 \\ \frac{da_2}{dt} &= -1.116a_1 + \underbrace{(0.218 - 0.27a_1^2 - 0.219a_2^2)}_{2\sigma(a_1, a_2)} a_2. \end{aligned} \quad (\text{A } 4)$$

Although it outperforms all of the other unconstrained models, model (A 4) suffers a major drawback : the amplitude of the limit cycle it predicts is different from unity (not shown). This misprediction of the amplitude results from the fact that, although the system is supposed to evolve onto the periodic orbit given, due to our normalization, by  $a_1^2 + a_2^2 = 1$ , the underbraced term in (A 4) does not vanish. Now knowing the structure of the model, we then add linear equality constraints in our identification problem (Loiseau & Brunton 2016) enforcing that the three parameters appearing in the instantaneous growth rate  $\sigma(a_1, a_2)$  are equal. Moreover, for the present flow configuration, the leading

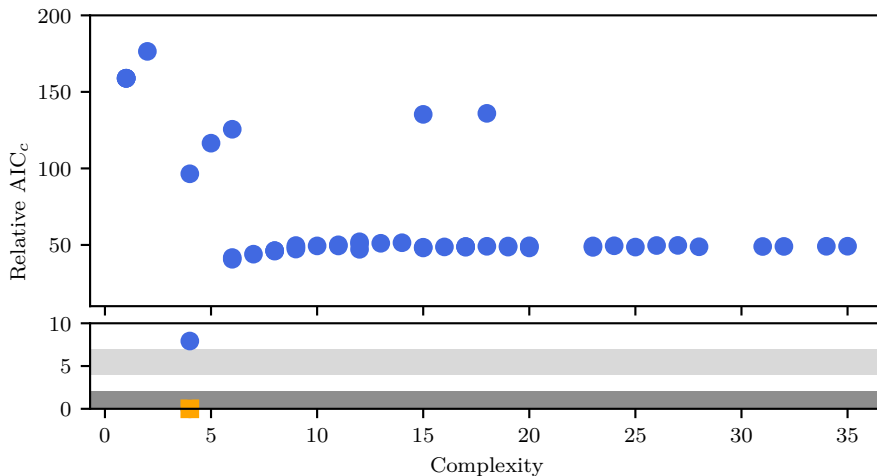


FIGURE 13. Relative AIC<sub>c</sub> criteria for models found by SINDy. The library of polynomial functions used for the identification includes up to 7<sup>th</sup> degree polynomials in  $a_1$  and  $a_2$ . Magnification in lower panel shows strong (dark gray) and weakly (light gray) supported AIC<sub>c</sub> range. The constrained cubic model (■) identified in §4.1 lies in the strong support range while its unconstrained counterpart lies just above the weakly supported range.

eigenvalue of the linearized Navier-Stokes operator can be computed by means of an Arnoldi time-stepping algorithm. For the computational domain and mesh considered, the real part of the leading eigenvalue is given by

$$\sigma_{NS} = 0.14.$$

Another linear equality constraint can then be added to the optimization procedure to enforce that the first parameter in (A 4) is equal to  $2\sigma_{NS}$ . The orange square in the lower panel of figure 13 corresponds to the model (4.3) presented in §4.1. Looking at its AIC ranking, it is clear that the constrained cubic model now outperforms all of the other identified models, even the unconstrained cubic one. This example clearly demonstrates how one can use SINDy (Brunton *et al.* 2016b) and model selection (Mangan *et al.* 2017) to identify the optimal structure of the model and then enhance the model performance by adding constraints derived from physical considerations (Loiseau & Brunton 2016) to the identification procedure.

## Appendix B. Identifying a discrete-time dynamical system

In this work, we have used the *Sparse Identification of Nonlinear Dynamics* (SINDy) algorithm, proposed by Brunton *et al.* (2016b), in order to identify a reduced-order model of the dynamics in the state  $\mathbf{a}$ . Given time-series of  $\mathbf{a}$  with a sufficiently small sampling period, the original SINDy algorithm allows us to identify the continuous-time dynamical system that governs the dynamics of  $\mathbf{a}$ . A number of alternative system identification techniques could also be used, such as the well-known Volterra series or NARMAX models (Billings 2013; Semeraro *et al.* 2016; Zhang *et al.* 2012; Glaz *et al.* 2010). However, these techniques assume a discrete-time representation of the dynamics of the form

$$\mathbf{a}^{(n+1)} = \mathbf{f}(\mathbf{a}^{(n)}).$$



Interestingly, the SINDy algorithm described in §3.2 only requires minor modifications in order to identify such systems. For that purpose, one simply needs to replace the matrix  $\dot{\mathbf{A}}$  in the optimization problem by a time-shifted copy of  $\mathbf{A}$ . Applying this strategy for the two-dimensional cylinder flow at  $Re = 100$  with a time-lag  $\tau = 0.125$  leads to the identification of the following discrete-time nonlinear dynamical system

$$\begin{bmatrix} a_1^{(n+1)} \\ a_2^{(n+1)} \end{bmatrix} = \begin{bmatrix} 0.994 & 0.139 \\ -0.122 & 1.026 \end{bmatrix} \begin{bmatrix} a_1^{(n)} \\ a_2^{(n)} \end{bmatrix} + \begin{bmatrix} 0 \\ -\left(0.019a_1^{(n)} + 0.04a_2^{(n)}\right) \left(a_1^{(n)}\right)^2 - \left(0.017a_1^{(n)} + 0.036a_2^{(n)}\right) \left(a_2^{(n)}\right)^2 \end{bmatrix}. \quad (\text{B } 1)$$

The resulting model can be interpreted as a sparse nonlinear vector autoregressive model (VAR) of the first order. As shown in figure 14, the time evolution of  $a_1(t)$  predicted by this low-dimensional discrete-time system is in good agreement with  $a_1^\bullet(t)$  based on a direct numerical simulation, whose initial condition has been chosen in the vicinity of the linearly unstable baseflow.

Based on the continuous-time system (4.3), it thus appears that SINDy can identify highly accurate low-order models of the two-dimensional cylinder flow. However, one may argue that direct numerical simulations only provide ideal noise-free and non-corrupted training data, hence questioning the ability of SINDy to identify similar low-dimensional systems from real-world experimental data. This issue can be addressed by pre-processing the training dataset, such as using a low-pass filter. Alternatively, Brunton *et al.* (2016b) used the *Total Variation Regularized Numerical Differentiation* proposed by Chartrand (2011) in order to evaluate the time-derivative of their noisy data prior to the identification step. Moreover, the SINDy implementation used by Brunton *et al.* (2016b), Loiseau & Brunton (2016) and herein relies on an iteratively hard-thresholded least-square algorithm. As such, one can easily estimate the variance-covariance matrix of the identified model's parameters in order to estimate its robustness even if noisy data are used. Finally, it has been shown by Tran & Ward (2016) that SINDy can exactly recover the governing equations even if the training data are highly corrupted, provided the system is sufficiently ergodic or if a sufficient number of different transient trajectories have been included in the training dataset.

## REFERENCES

- AKAIKE, H. 1974 A new look at the statistical model identification. *Automatic Control, IEEE Transactions on* **19** (6), 716–723.
- ARBABI, H. & MEZIĆ, I. 2016 Ergodic theory, Dynamic Mode Decomposition and Computation of Spectral Properties of the Koopman operator. *arXiv preprint arXiv:1611.06664*.
- AUBRY, N., HOLMES, P., LUMLEY, J. L. & STONE, E. 1988 The dynamics of coherent structures in the wall region of a turbulent boundary layer. *J. Fluid Mech.* **192**, 115–173.
- BABAEI, H. & SAPSIS, T. P. 2016 A variational principle for the description of time-dependent modes associated with transient instabilities. *Phil. Trans. Roy. Soc. Lond.* **accepted**.
- BAGHERI, S. 2013 Koopman-mode decomposition of the cylinder wake. *J. Fluid Mech* **726**, 596–623.
- BALAJEWICZ, M., DOWELL, E. H. & NOACK, B. R. 2013 Low-dimensional modelling of high-Reynolds-number shear flows incorporating constraints from the Navier-Stokes equation. *J. Fluid Mech.* **729**, 285–308.
- BARKLEY, D. & HENDERSON, R. D. 1996 Three-dimensional Floquet stability analysis of the wake of a circular cylinder. *J. Fluid Mech.* **322**, 215–241.

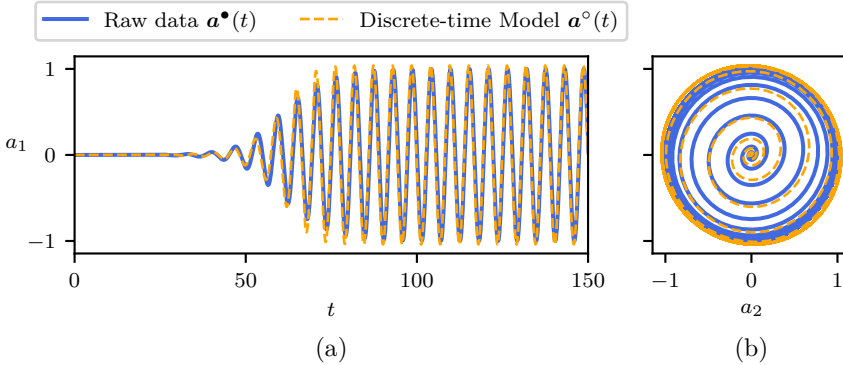


FIGURE 14. (a) Comparison of the evolution as a function of time of the sensor measurement  $a_1$  obtained from direct numerical simulation (—  $\mathbf{a}_1^\bullet$ ) and predicted by the discrete-time sparse model (---  $\mathbf{a}_1^\circ$ ). (b) Trajectory of the true and identified systems in the phase plane ( $a_1, a_2$ ). In both cases, the initial condition is close to the linearly unstable fixed point.

- BARNETT, T. P. & HASSELMANN, K. 1979 Techniques of linear prediction, with application to oceanic and atmospheric fields in the tropical Pacific. *Rev. Geophys.* **17**, 949–968.
- BERKOOZ, G., HOLMES, P. J. & LUMLEY, J. L. 1993 The proper orthogonal decomposition in the analysis of turbulent flows. *Annual review of fluid mechanics* **25** (1), 539–575.
- BILLINGS, S. A. 2013 *Nonlinear system identification: NARMAX methods in the time, frequency, and spatio-temporal domains*. John Wiley & Sons.
- BONGARD, J. & LIPSON, H. 2007 Automated reverse engineering of nonlinear dynamical systems. *Proceedings of the National Academy of Sciences* **104** (24), 9943–9948.
- BOURGUET, R., BRAZA, M. & DERVIEUX, A. 2011 Reduced-order modeling of transonic flows around an airfoil submitted to small deformations. *J. Comp. Phys.* **230**, 159–184.
- BRUNTON, S. L., BRUNTON, B. W., PROCTOR, J. L., KAISER, E. & KUTZ, J. N. 2017 Chaos as an intermittently forced linear system. *Nature Communications* **8** (19), 1–9.
- BRUNTON, S. L., BRUNTON, B. W., PROCTOR, J. L. & KUTZ, J. N. 2016a Koopman invariant subspaces and finite linear representations of nonlinear dynamical systems for control. *PLoS ONE* **11** (2), e0150171.
- BRUNTON, S. L., DAWSON, S. T. M. & ROWLEY, C. W. 2014 State-space model identification and feedback control of unsteady aerodynamic forces. *Journal of Fluids and Structures* **50**, 253–270.
- BRUNTON, S. L. & NOACK, B. R. 2015 Closed-loop turbulence control: Progress and challenges. *Applied Mechanics Reviews* **67** (5), 050801.
- BRUNTON, S. L., PROCTOR, J. L. & KUTZ, J. N. 2016b Discovering governing equations from data by sparse identification of nonlinear dynamical systems. *Proceedings of the National Academy of Sciences* **113** (15), 3932–3937.
- BRUNTON, S. L., PROCTOR, J. L. & KUTZ, J. N. 2016c Sparse Identification of Nonlinear Dynamics with Control (SINDYc). *IFAC NOLCOS* **49** (18), 710–715.
- BRUNTON, S. L., ROWLEY, C. W. & WILLIAMS, D. R. 2013 Reduced-order unsteady aerodynamic models at low Reynolds numbers. *Journal of Fluid Mechanics* **724**, 203–233.
- CANDÈS, E. J. 2006 Compressive sensing. *Proceedings of the International Congress of Mathematics*.
- CARLBERG, K., BARONE, M. & ANTIL, H. 2017 Galerkin v. least-squares Petrov–Galerkin projection in nonlinear model reduction. *Journal of Computational Physics* **330**, 693–734.
- CARLBERG, K., TUMINARO, R. & BOGGS, P. 2015 Preserving Lagrangian structure in nonlinear model reduction with application to structural dynamics. *SIAM Journal on Scientific Computing* **37** (2), B153–B184.

- CHARTRAND, R. 2011 Numerical differentiation of noisy, nonsmooth data. *ISRN Applied Mathematics* **2011**.
- COLEBROOK, J. M. 1978 Continuous plankton records: Zooplankton and environment, Northeast Atlantic and North Sea. *Oceanol. Acta* **1**, 9–23.
- CORDIER, L., NOACK, B. R., DAVILLER, G., DELVILLE, J., LEHNASCH, G., TISSOT, G., BALAJEWICZ, M. & NIVEN, R.K. 2013 Control-oriented model identification strategy. *Exp. Fluids* **54**, Article 1580.
- DEANE, A. E., KEVREKIDIS, I. G., KARNIADAKIS, G. E. & ORSZAG, S. A. 1991 Low-dimensional models for complex geometry flows: Application to grooved channels and circular cylinders. *Phys. Fluids A* **3**, 2337–2354.
- DONOHO, D. L. 2006 Compressed sensing. *IEEE Transactions on Information Theory* **52** (4), 1289–1306.
- DULLERUD, GEIR. E. & PAGANINI, F. 2000 *A course in robust control theory: A convex approach*. Berlin, Heidelberg: Springer.
- DURIEZ, T., BRUNTON, S. L. & NOACK, B. R. 2016 Machine Learning Control–Taming Nonlinear Dynamics and Turbulence. *Fluid mechanics and its applications (ISSN 0926-5112)* **116**.
- FABBIANE, N., SEMERARO, O., BAGHERI, S. & HENNINGSON, D. S. 2014 Adaptive and model-based control theory applied to convectively unstable flows. *Applied Mechanics Reviews* **66** (6), 060801.
- FEYNMAN, R. P., LEIGHTON, R. B. & SANDS, M. 2013 *The Feynman Lectures on Physics*, , vol. 2. Basic Books.
- FISCHER, P.F., LOTTES, J.W. & KERKEMEIR, S.G. 2008 Nek5000 Web pages. [Http://nek5000.mcs.anl.gov](http://nek5000.mcs.anl.gov).
- GALLETTI, G., BRUNEAU, C. H., ZANNETTI, L. & IOLLO, A. 2004 Low-order modelling of laminar flow regimes past a confined square cylinder. *J. Fluid Mech.* **503**, 161–170.
- Ghil, M., ALLEN, R. M., DETTINGER, M. D., IDE, K., KONDRASHOV, D. & OTHERS 2002 Advanced spectral methods for climatic time series. *Rev. Geophys.* **40**, 3.1–3.41.
- GLAZ, B., LIU, L. & FRIEDMANN, P. P. 2010 Reduced-order nonlinear unsteady aerodynamic modeling using a surrogate-based recurrence framework. *AIAA journal* **48** (10), 2418–2429.
- GRAHAM, W. R., PERAIRE, J. & TANG, K. Y. 1999 Optimal control of vortex shedding usind low-order models. Part I — Open-loop model development. *Int. J. Numer. Meth. Engrng.* **44**, 945–972.
- HEMATI, M. S., DAWSON, S. TM & ROWLEY, C. W. 2016 Parameter-Varying Aerodynamics Models for Aggressive Pitching-Response Prediction. *AIAA Journal* pp. 1–9.
- HOLMES, P. J. & GUCKENHEIMER, J. 1983 *Nonlinear oscillations, dynamical systems, and bifurcations of vector fields, Applied Mathematical Sciences*, vol. 42. Berlin, Heidelberg: Springer-Verlag.
- HOLMES, P. J., LUMLEY, J. L., BERKOOZ, G. & ROWLEY, C. W. 2012 *Turbulence, coherent structures, dynamical systems and symmetry*, 2nd edn. Cambridge, England: Cambridge University Press.
- HOSSEINI, Z., NOACK, B. R. & MARTINUZZI, R. J. 2016 Modal energy flow analysis of a highly modulated wake behind a wall-mounted pyramid. *J. Fluid Mech.* **798**, 774–786.
- JUANG, J.-N. & PAPPA, R. S. 1985 An eigensystem realization algorithm for modal parameter identification and model reduction. *Journal of guidance, control, and dynamics* **8** (5), 620–627.
- KAISER, E., NOACK, B. R., CORDIER, L., SPOHN, A., SEGOND, M., ABEL, M., DAVILLER, G., OSTH, J., KRAJNOVIC, S. & NIVEN, R. K. 2014 Cluster-based reduced-order modelling of a mixing layer. *J. Fluid Mech.* **754**, 365–414.
- KALMAN, R. E. 1960 A new approach to linear filtering and prediction problems. *Journal of Fluids Engineering* **82** (1), 35–45.
- KRIZHEVSKY, A., SUTSKEVER, I. & HINTON, G. E. 2012 Imagenet classification with deep convolutional neural networks. In *Advances in neural information processing systems*, pp. 1097–1105.
- KUTZ, J. N. 2017 Deep learning in fluid dynamics. *Journal of Fluid Mechanics* **814**, 1–4.

- KUTZ, J. N., BRUNTON, S. L., BRUNTON, B. W. & PROCTOR, J. L. 2016 *Dynamic Mode Decomposition: Data-Driven Modeling of Complex Systems*. SIAM.
- LEE, C., KIM, J., BABCOCK, D. & GOODMAN, R. 1997 Application of neural networks to turbulence control for drag reduction. *Physics of Fluids* **9** (6), 1740–1747.
- LING, J., KURZAWSKI, A. & TEMPLETON, J. 2016 Reynolds averaged turbulence modelling using deep neural networks with embedded invariance. *Journal of Fluid Mechanics* **807**, 155–166.
- LOISEAU, J.-CH. & BRUNTON, S. L. 2016 Constrained sparse Galerkin regression. *arXiv preprint arXiv:1611.03271*.
- MANGAN, N. M., BRUNTON, S. L., PROCTOR, J. L. & KUTZ, J. N. 2016 Inferring biological networks by sparse identification of nonlinear dynamics. *IEEE Transactions on Molecular, Biological, and Multi-Scale Communications* **2** (1), 52–63.
- MANGAN, N. M., KUTZ, J. N., BRUNTON, S. L. & PROCTOR, J. L. 2017 Model selection for dynamical systems via sparse regression and information criteria. *arXiv preprint arXiv:1701.01773*.
- MANTIĆ-LUGO, V., ARRATIA, C. & GALLAIRE, F. 2014 Self-consistent mean flow description of the nonlinear saturation of the vortex shedding in the cylinder wake. *Physical review letters* **113** (8), 084501.
- MC CONAGHY, T. 2011 Ffx: Fast, scalable, deterministic symbolic regression technology. In *Genetic Programming Theory and Practice IX*, pp. 235–260. Springer.
- MEZIĆ, I. 2005 Spectral properties of dynamical systems, model reduction and decompositions. *Nonlinear Dynamics* **41** (1-3), 309–325.
- MEZIĆ, I. 2013 Analysis of fluid flows via spectral properties of the Koopman operator. *Annual Review of Fluid Mechanics* **45**, 357–378.
- MILANO, M. & KOUMOUTSAKOS, P. 2002 Neural network modeling for near wall turbulent flow. *Journal of Computational Physics* **182** (1), 1–26.
- NAIR, A. G. & TAIRA, K. 2015 Network-theoretic approach to sparsified discrete vortex dynamics. *Journal of Fluid Mechanics* **768**, 549–571.
- NOACK, B. R. 2016 From snapshots to modal expansions – bridging low residuals and pure frequencies. *J. Fluid Mech. – Focus in Fluids* **802**, 1–4.
- NOACK, B. R., AFANASIEV, K., MORZYŃSKI, M., TADMOR, G. & THIELE, F. 2003 A hierarchy of low-dimensional models for the transient and post-transient cylinder wake. *J. Fluid Mech.* **497**, 335–363.
- NOACK, B. R., MORZYŃSKI, M. & TADMOR, G. 2011 *Reduced-order modelling for flow control.*, vol. 528. Springer Science & Business Media.
- NOACK, B. R., STANKIEWICZ, W., MORZYŃSKI, M. & SCHMID, P. J. 2016 Recursive dynamic mode decomposition of transient and post-transient wake flows. *J. Fluid Mech.* **809**, 843–872.
- ÖSTH, J., KRAJNOVIĆ, S., NOACK, B. R., BARROS, D. & BORÉE, J. 2014 On the need for a nonlinear subscale turbulence term in POD models as exemplified for a high Reynolds number flow over an Ahmed body. *J. Fluid Mech.* **747**, 518–544.
- REDINIOTIS, O.K., KO, J. & KURDILA, A.J. 2002 Reduced order nonlinear Navier-Stokes models for synthetic jets. *J. Fluids Enrg.* **124** (2), 433–443.
- REMPFER, D. 2000 On low-dimensional Galerkin models for fluid flow. *Theoret. Comput. Fluid Dynamics* **14**, 75–88.
- REMPFER, D. & FASEL, F. H. 1994 Dynamics of three-dimensional coherent structures in a flat-plate boundary-layer. *J. Fluid Mech.* **275**, 257–283.
- ROWLEY, C. W. & DAWSON, S. 2016 Model reduction for flow analysis and control. *Annual Review of Fluid Mechanics* **49** (1).
- ROWLEY, C. W., MEZIĆ, I., BAGHERI, S., SCHLATTER, P. & HENNINGSON, D.S. 2009 Spectral analysis of nonlinear flows. *J. Fluid Mech.* **645**, 115–127.
- RUDY, S. H., BRUNTON, S. L., PROCTOR, J. L. & KUTZ, J. N. 2017 Data-driven discovery of partial differential equations. *Science Advances* **3** (e1602614).
- SCHAEFFER, H. 2017 Learning partial differential equations via data discovery and sparse optimization. In *Proc. R. Soc. A*, , vol. 473, p. 20160446.
- SCHLEGEL, M. & NOACK, B. R. 2015 On long-term boundedness of galerkin models. *Journal of Fluid Mechanics* **765**, 325–352.

- SCHMID, P. J. 2010 Dynamic mode decomposition of numerical and experimental data. *Journal of Fluid Mechanics* **656**, 5–28.
- SCHMIDT, M. & LIPSON, H. 2009 Distilling free-form natural laws from experimental data. *science* **324** (5923), 81–85.
- SCHÖLKOPF, B., SMOLA, A. & MULLER, K.-R. 1998 Nonlinear component analysis as a kernel eigenvalue problem. *Neural Computation* **10**, 1299–1319.
- SCHUMM, M., EBERHARD, B. & MONKEWITZ, P. A. 1994 Self-excited oscillations in the wake of two-dimensional bluff bodies and their control. *J. Fluid Mech.* **271**, 17–53.
- SCHWARZ, G. & OTHERS 1978 Estimating the dimension of a model. *The annals of statistics* **6** (2), 461–464.
- SEMERARO, O., LUSSEYRAN, F., PASTUR, L. & JORDAN, P. 2016 Qualitative dynamics of wavepackets in turbulent jets. *arXiv preprint arXiv:1608.06750*.
- SENGUPTA, T. K., HAIDER, S. I., PARVATHI, M. K. & PALLAVI, G. 2015 Enstrophy-based proper orthogonal decomposition for reduced-order modeling of flow past a cylinder. *Physical Review E* **91** (4), 043303.
- SIPP, D. & SCHMID, P. J. 2016 Linear closed-loop control of fluid instabilities and noise-induced perturbations: A review of approaches and tools. *Applied Mechanics Reviews* **68** (2), 020801.
- SIROVICH, L. 1987 Turbulence and the dynamics of coherent structures. Part I: Coherent structures. *Quarterly of Applied Mathematics* **45** (3), 561–571.
- SKOGESTAD, S. & POSTLETHWAITE, I. 2005 *Multivariable feedback control: analysis and design*, 2nd edn. Hoboken, New Jersey: John Wiley & Sons, Inc.
- TADMOR, G., LEHMANN, O., NOACK, B. R., CORDIER, L., DELVILLE, J., BONNET, J.-P. & MORZYŃSKI, M. 2011 Reduced order models for closed-loop wake control. *Philosophical Transactions of the Royal Society A* **369** (1940), 1513–1524.
- TADMOR, G., LEHMANN, O., NOACK, B. R. & MORZYŃSKI, M. 2010 Mean field representation of the natural and actuated cylinder wake. *Physics of Fluids (1994-present)* **22** (3), 034102.
- TAKENS, F. 1981 Detecting strange attractors in turbulence. In *Dynamical systems and turbulence, Warwick 1980*, pp. 366–381. Springer.
- TIBSHIRANI, R. 1996 Regression shrinkage and selection via the lasso. *Journal of the Royal Statistical Society. Series B (Methodological)* pp. 267–288.
- TRAN, G. & WARD, R. 2016 Exact Recovery of Chaotic Systems from Highly Corrupted Data. *ArXiv e-prints*, arXiv: 1607.01067.
- TU, J. H., ROWLEY, C. W., LUCHTENBURG, D. M., BRUNTON, S. L. & KUTZ, J. N. 2014 On dynamic mode decomposition: theory and applications. *Journal of Computational Dynamics* **1** (2), 391–421.
- UKEILEY, L., CORDIER, L., MANCEAU, R., DELVILLE, J., BONNET, J. P. & GLAUSER, M. 2001 Examination of large-scale structures in a turbulent plane mixing layer. Part 2. Dynamical systems model. *J. Fluid Mech.* **441**, 61–108.
- WANG, W. X., YANG, R., LAI, Y. C., KOVANIS, V. & GREBOGI, C. 2011 Predicting catastrophes in nonlinear dynamical systems by compressive sensing. *Physical Review Letters* **106**, 154101–1–154101–4.
- WEARE, B. C. & NASSTROM, J. N. 1982 Examples of extended empirical orthogonal function analyses. *Mon. Weather Rev.* **110**, 784–812.
- WEI, M. & ROWLEY, C. W. 2009 Low-dimensional models of a temporally evolving free shear layer. *J. Fluid Mech* **618**, 113–134.
- WELCH, G. & BISHOP, G. 1995 An introduction to the Kalman filter.
- WIENER, N. 1948 *Cybernetics or Control and Communication in the Animal and the Machine*, 1st edn. Boston: MIT Press.
- WILLIAMS, M. O., KEVREKIDIS, I. G. & ROWLEY, C. W. 2015 A data-driven approximation of the Koopman operator: extending dynamic mode decomposition. *Journal of Nonlinear Science*.
- ZEBIB, A. 1987 Stability of viscous flow past a circular cylinder. *Journal of Engineering Mathematics* **21** (2), 155–165.
- ZHANG, H.-Q., FEY, U., NOACK, B. R., KÖNIG, M. & ECKELMANN, H. 1995 On the transition of the cylinder wake. *Physics of Fluids (1994-present)* **7** (4), 779–794.

- ZHANG, W., WANG, B., YE, Z. & QUAN, J. 2012 Efficient method for limit cycle flutter analysis based on nonlinear aerodynamic reduced-order models. *AIAA journal* **50** (5), 1019–1028.
- ZHANG, Z. J. & DURAISAMY, K. 2015 Machine learning methods for data-driven turbulence modeling. In *22nd AIAA Computational Fluid Dynamics Conference*, p. 2460.